JFM PAPERS

Diagnosing tracer transport in convective penetration of a stably stratified layer

Charles W. Powell[1][†], **Peter H. Haynes**[1] **and John R. Taylor**[1]

[1]Department of Applied Mathematics and Theoretical Physics, University of Cambridge, Centre for Mathematical Sciences, Wilberforce Road, Cambridge CB3 0WA, UK

We use large-eddy simulations to study the penetration of a buoyant plume carrying a passive tracer into a stably stratified layer with constant buoyancy frequency. Using a buoyancy-tracer volume distribution, we develop a method for objectively partitioning plume fluid in buoyancy-tracer space into three regions, each of which corresponds to a coherent region in physical space. Specifically, we identify a source region where undiluted plume fluid enters the stratified layer, a transport region where much of the transition from undiluted to mixed fluid occurs in the plume cap and an accumulation region corresponding to a radially spreading intrusion. This method enables quantification of different measures of turbulence and mixing within each of the three regions, including potential energy and turbulent kinetic energy dissipation rates, an activity parameter and the instantaneous mixing efficiency. We find that the most intense buoyancy gradients lie in a thin layer at the cap of the penetrating plume. This provides the primary stage of mixing between plume and environment and exhibits a mixing efficiency around 50 %. Newly generated mixtures of environmental and plume fluid join the intrusion and experience relatively weak turbulence and buoyancy gradients. As the intrusion spreads radially, environmental fluid surrounding the intrusion is mixed into the intrusion with moderate mixing efficiency. This dominates the volume of environmental fluid entrained into the region containing plume fluid. However, the 'strongest' entrainment, as measured by the specific entrainment rate, is largest in the plume cap, where the most buoyant environmental fluid is entrained.

Key words: plumes/thermals, stratified flows, turbulent mixing

† Email address for correspondence: cwp29@cam.ac.uk

1. Introduction

The interaction between active convection and neighbouring stably stratified regions is relevant to many geophysical flows. An important example is the tropical upper troposphere and lower stratosphere, where convective plumes generated by strong thunderstorm complexes can penetrate through the tropical tropopause layer into the lower stratosphere, resulting in vertical transport of trace gases and water vapour (Jensen, Ackerman & Smith 2007; Randel & Jensen 2013). Numerical simulations of convective penetration events have been performed using realistic and complex meteorological models (Dauhut *et al.* 2015, 2018) containing many physical processes but these are computationally expensive and challenging to interpret.

Another geophysical process where this fluid dynamical problem is relevant is deep convection in the open ocean. Typically, mixing between the deep ocean and near-surface water is hindered by the strong vertical density gradients of the thermocline. In some regions, including several locations in high latitude oceans and the Mediterranean Sea, intense buoyancy loss from the ocean surface to the atmosphere results in strong, deep-reaching convection (Marshall & Schott 1999; Herrmann *et al.* 2008). The transport of surface water into the deep ocean sets and maintains the properties of the abyss (Marshall & Schott 1999), both in terms of the general circulation and also biogeochemical cycles (Ulses *et al.* 2021).

Further examples of naturally occurring flows involving penetrative convection include modification of downslope oceanic gravity currents by near-surface convection (Doda *et al.* 2023), smaller-scale atmospheric convection below an inversion (Kurbatskii 2001), volcanic eruptions that penetrate into the stratosphere (e.g. Textor *et al.* 2003; Carazzo, Kaminski & Tait 2008) as well as the internal structure of many stars where a convectively unstable layer is bounded above and below by stable layers (Singh, Roxburgh & Chan 1994; Masada, Yamada & Kageyama 2013). Moreover, the fluid dynamical problem of convective penetration itself is of continuing scientific interest, in particular the generation of gravity waves by the penetrating plume cap (Ansong & Sutherland 2010) and the energetics of the system (Chen & Bhaganagar 2023), with applications to many problems – see Hunt & Burridge (2015) for a discussion of open questions on fountains, i.e. plumes surrounded by a more buoyant environment. Much previous work has focused on laboratory studies of buoyant plumes with simple background density profiles, but numerical simulation has recently become feasible (Alfonsi 2011).

Progress towards understanding the contribution of convective penetration to tracer transport in geophysical settings can be made by considering an idealised representation of the problem in which a region of strong stable stratification is penetrated by a turbulent buoyant plume generated in a region with weak or zero stratification. The objective of the study reported in this paper is to diagnose the irreversible diapycnal tracer transport that results from turbulent mixing between plume fluid carrying a passive tracer and the surrounding environmental fluid in the stratified layer. We aim to provide a quantitative description of the mixing involved in this diapycnal transport. Such descriptions are essential in forming parameterisations of convective penetration. Throughout the flow evolution, plume fluid may be distinguished from environmental fluid by the presence of non-zero tracer concentration. Crucially, both the tracer concentration and buoyancy fields are subjected to turbulent mixing, resulting in the entrainment of environmental fluid into the plume and modification of the relationship between buoyancy and tracer within the plume. Plumb (2007) introduced a tracer–tracer probability density function to study rapid isentropic mixing in the stratosphere. Penney *et al.* (2020) utilised this method to study diapycnal mixing of passive tracers by Kelvin–Helmholtz billows arising in a
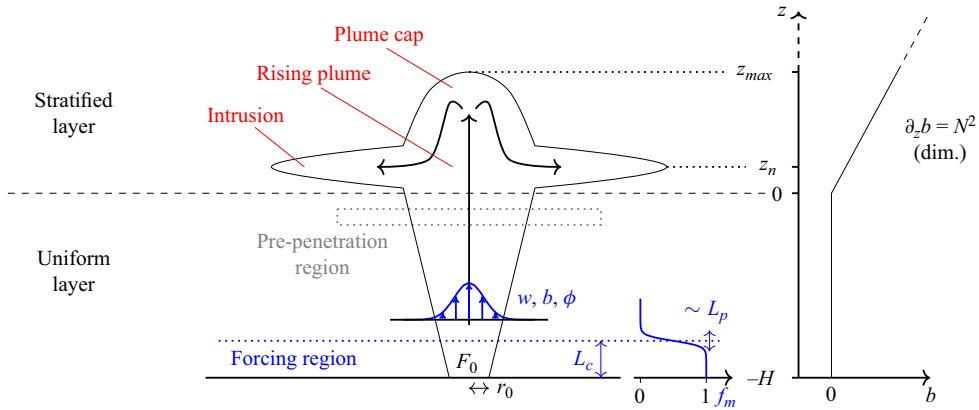
Figure 1. Set-up for numerical simulations of a buoyant plume with source integral buoyancy and tracer flux F_0 and source radius r_0 penetrating from a uniform layer into a linearly stably stratified layer with constant buoyancy frequency N. The main plume structures discussed throughout this paper are indicated in red. The pre-penetration region defined in § 3 for diagnostic purposes is shown in grey. The initial buoyancy profile (right) in the stratified environment is $b(x, 0) = N^2 z$ (dimensional) for $z \geqslant 0$. The maximum penetration height z_{max} and intrusion height z_n above the bottom of the stratified layer are indicated by dotted lines. We also show the forcing region of depth L_c and the forcing modulation profile $f_m(z)$ decaying over a distance L_p in blue, detailed in Appendix A. The (azimuthally averaged) Gaussian profiles of w, b and ϕ in the plume rising through the uniform layer are also illustrated in blue.

stratified shear flow. Using buoyancy as one of the tracers, the redistribution of fluid in buoyancy-tracer space was used to interpret the mixing process.

In this paper we use a similar formulation to diagnose the diapycnal transport of a passive tracer in a buoyant plume penetrating a linearly stably stratified layer. The numerical method is detailed in § 2. The evolution of the flow and tracer concentration is presented in § 3. In § 4 we introduce our formulation of the buoyancy-tracer 'volume distribution'. We show that the flow can be partitioned into three regions of buoyancy-tracer space: the source region where plume fluid enters the stratified layer, a transport region through which volume flows during initial mixing between the plume and environment and an accumulation region where mixed fluid settles and homogenises. Each of these regions of buoyancy-tracer space correspond to coherent regions of physical space that identify the essential structures of the flow, namely the rising plume, plume cap and radially spreading intrusion, respectively. These structures are indicated in figure 1. In § 5 we analyse diagnostics of the mixing process in each of these regions.

2. Governing equations and numerical model

We consider the penetration of a buoyant plume with source radius r_0 and source integral buoyancy flux F_0 generated in a uniform layer of depth H into a stably stratified layer with buoyancy frequency N. The problem set-up is shown in figure 1. To aid in the examination of the flow evolution and mixing, we include a passive tracer ϕ that satisfies the same evolution equation as buoyancy $b = -g\rho'/\rho_0$ where ρ' is the density deviation from a reference value ρ_0. The tracer is passive in the sense that it has no coupling with the momentum equation. The scalar field $\phi(x, t)$ represents the (dimensionless) tracer concentration normalised by the tracer concentration on the plume centreline at the source. As illustrated in figure 1, we define the bottom of the initial stratified layer to be $z = 0$. We also define $t = 0$ as the time at which the plume first penetrates into the stratified

Re	Pr	r_0	H	L_{domain}	L_c	L_p	τ
6.29×10^6	0.70	0.20	7.97	23.9	0.80	0.40	1.00

Table 1. Non-dimensional parameters for the LES with $N = 1$ s^{-1} and $F_0 = 3.96 \times 10^{-7}$ m^4 s^{-3} discussed from § 3 onwards.

layer. The plume source (at the base of the domain) lies at $z = -H \approx -7.97$ for the parameter choices given in table 1. The initial conditions are $\phi(\boldsymbol{x}, 0) = 0$ throughout the domain whilst $b(\boldsymbol{x}, 0) = 0$ in the uniform layer $z \leqslant 0$ and $b(\boldsymbol{x}, 0) = N^2 z$ (dimensional) in the stratified layer $z \geqslant 0$.

We generate the buoyant plume by forcing the vertical velocity w, buoyancy b and tracer concentration ϕ in the shallow forcing region of depth L_c indicated in figure 1. The plume centreline lies at the middle of the computational domain, $x = y = 0$. Details on the plume forcing method can be found in Appendix A. At the source, the generated plume has integral buoyancy flux $F_0 = 2 \int_0^\infty \bar{w}\bar{b}|_{z=-H} r \, dr$, where $\bar{\cdot}$ denotes an azimuthal and time average, with no excess momentum flux (i.e. a 'pure' plume, see Appendix A for detail). Turbulence is initiated in the plume by applying a 10 % perturbation to the forcing profiles in the forcing region and to all velocity components in the two grid layers above the forcing region. Turbulence develops as the plume rises through the uniform layer and we ensure that, prior to penetrating the stratified layer, the azimuthally averaged vertical velocity, buoyancy and tracer concentration are self-similar with a Gaussian radial profile as expected in a fully developed plume (see Appendices A and B).

We non-dimensionalise using the source integral buoyancy flux F_0 (with dimensions $L^4 T^{-3}$) and buoyancy frequency N in the stable layer. The length scale is $L = F_0^{1/4} N^{-3/4}$ and the time scale is $T = N^{-1}$. We assume the velocity scale is L/T. The length scale L naturally arises from the Morton, Taylor & Turner (1956) plume equations in a stably stratified environment. Following previous experimental and numerical studies (e.g. Briggs 1965; Devenish, Rooney & Thomson 2010), both the maximum height of the plume z_{max} and the height of the intrusion z_n above the base of the stratification (illustrated in figure 1) scale with L (in the case of a 'lazy' plume, when incident momentum is negligible, as considered here).

Owing to the large range of length scales involved in convective penetration, resolving turbulent scales with direct numerical simulation is not feasible due to the computational cost of very high resolution simulations. We therefore use large-eddy simulation (LES) with the anisotropic minimum dissipation (AMD) eddy-viscosity model to represent unresolved scales (Vreugdenhil & Taylor 2018). Large-eddy simulation has been shown to be effective for simulating plumes in previous work in the literature, e.g. Pham, Plourde & Doan (2007). The non-dimensional governing equations for velocity $\boldsymbol{u}$ and scalars b, ϕ including sub-grid-scale (SGS) contributions are

$$\nabla \cdot \hat{\boldsymbol{u}} = 0, \tag{2.1}$$

$$\frac{D\hat{\boldsymbol{u}}}{Dt} + \nabla \hat{p} = \frac{1}{Re} \nabla^2 \hat{\boldsymbol{u}} + \hat{b}\hat{\boldsymbol{k}} - \nabla \cdot \boldsymbol{\tau} + f_w \hat{\boldsymbol{k}}, \tag{2.2}$$

$$\frac{D\hat{b}}{Dt} = \frac{1}{RePr} \nabla^2 \hat{b} - \nabla \cdot \boldsymbol{\lambda}_b + f_b, \tag{2.3}$$

$$\frac{\mathrm{D}\hat{\phi}}{\mathrm{D}t} = \frac{1}{RePr}\nabla^2\hat{\phi} - \boldsymbol{\nabla}\cdot\boldsymbol{\lambda}_\phi + f_\phi, \tag{2.4}$$

where $\hat{\;}$ indicates filtering at the resolved grid scale and $\hat{\boldsymbol{k}}$ is the unit vector in the vertical direction. The terms f_w, f_b and f_ϕ represent the forcing applied to the vertical velocity, buoyancy and passive tracer to generate the buoyant plume. The details of this forcing are discussed in Appendix A. The SGS stress tensor $\boldsymbol{\tau}$ has components $\tau_{ij} = \widehat{u_iu_j} - \hat{u}_i\hat{u}_j$, the SGS buoyancy flux is $\boldsymbol{\lambda}_b = \widehat{\boldsymbol{u}b} - \hat{\boldsymbol{u}}\hat{b}$ and similarly the SGS tracer flux is $\boldsymbol{\lambda}_\phi = \widehat{\boldsymbol{u}\phi} - \hat{\boldsymbol{u}}\hat{\phi}$. The two dimensionless parameters are the Reynolds number and Prandtl number

$$Re = \frac{F_0^{1/2}}{\nu N^{1/2}}, \quad Pr = \frac{\nu}{\kappa}, \tag{2.5a,b}$$

respectively, where ν is the molecular viscosity and κ is the molecular diffusivity for both b and ϕ. The eddy-viscosity model for the deviatoric component of the SGS stress $\boldsymbol{\tau}^d$ and the SGS buoyancy and tracer flux are

$$\tau_{ij}^d = \tau_{ij} - \tfrac{1}{3}\delta_{ij}\tau_{kk} = -2\nu_{SGS}\hat{S}_{ij}, \quad \boldsymbol{\lambda}_b = -\kappa_{SGS}^{(b)}\boldsymbol{\nabla}\hat{b}, \quad \boldsymbol{\lambda}_\phi = -\kappa_{SGS}^{(\phi)}\boldsymbol{\nabla}\hat{\phi}, \tag{2.6a–c}$$

where ν_{SGS}, $\kappa_{SGS}^{(b)}$ and $\kappa_{SGS}^{(\phi)}$ are the non-dimensional SGS viscosity, SGS buoyancy diffusivity and SGS tracer diffusivity, respectively, each determined by the AMD scheme. The term $\hat{S}_{ij}$ is the components of the non-dimensional shear-rate tensor. The SGS diffusivities and viscosity may locally exceed the molecular values by several orders of magnitude in regions with intense turbulence.

We use DIABLO (Taylor 2008) to perform three-dimensional LES of the idealised set-up shown in figure 1. DIABLO evolves the Boussinesq Navier–Stokes equations (2.1)–(2.4) discretised using Fourier modes in the two periodic horizontal directions and second-order finite differences in the vertical direction. The boundary conditions on the top and bottom boundary are $\partial_z u = \partial_z v = \partial_z b = \partial_z \phi = 0$ and $w = 0$. A third-order Runge–Kutta scheme is used for time stepping. A 2/3 dealiasing rule is applied when transforming from Fourier to physical space. We use a cubic domain of side length L_{domain} with a uniform grid of $512^2 \times 513$ points. The side length is chosen large enough that edge effects are not present and the radially spreading intrusion that forms does not reach the boundary during the simulation. A sponge layer is added in the top 20 % of the domain (which the simulated plume does not reach), where the velocity is damped towards zero and the buoyancy is damped towards the initial background stratification $b(\boldsymbol{x}, 0) = z$ (non-dimensional), to inhibit the reflection of internal gravity waves from the top boundary. Validation of the numerical method discussed here is detailed in Appendix B.

Henceforth we refer to a single simulation with parameters which are equivalent to the experimental set-up used by Ansong & Sutherland (2010) except for the source buoyancy flux, which is weaker here. The parameters are given in table 1 and non-dimensionalised by $N = 1 \text{ s}^{-1}$ and $F_0 = 3.96 \times 10^{-7} \text{ m}^4 \text{ s}^{-3}$. Henceforth, all values stated are non-dimensionalised with respect to this choice of F_0 and N. We also drop the hat notation and refer to the resolved variables unless otherwise noted.

3. Flow and tracer structure

The flow evolution is presented in three vertical cross-sections through the plume centreline in figure 2. We identify the plume as regions with tracer concentration
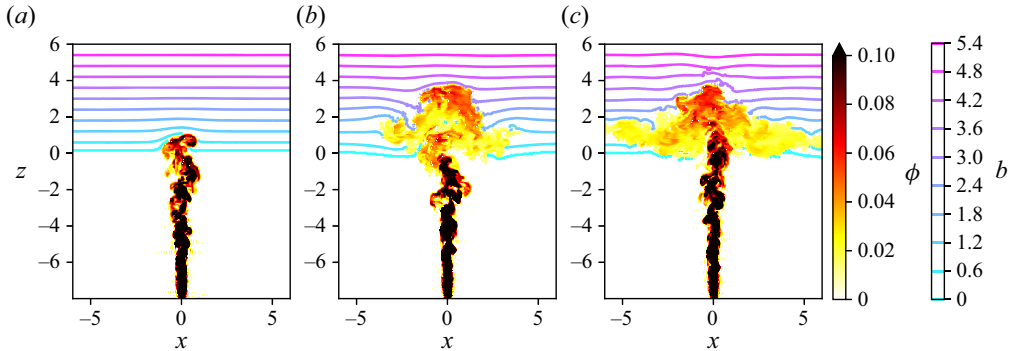
Figure 2. Three stages of the flow evolution, shown as $x - z$ cross-sections of the tracer concentration ϕ shown where ϕ exceeds 1 % of its value on the plume centreline at the source $z = -H$. Buoyancy contours are shown otherwise. Cross-sections are taken at the plume centreline at non-dimensional times $t = 1, 6.75, 14$. From left to right, the panels show the plume during initial penetration, reaching maximum penetration height and spreading of the intrusion.

$\phi \geqslant \phi_{min} \equiv 10^{-2}$, i.e. we threshold the tracer field at 1 % of its value on the plume centreline at the source. In the tracer-less environment surrounding the plume we show contours of the buoyancy field. The bottom of the stratified layer, above which the buoyancy of the environment becomes non-zero, is indicated by the lowest buoyancy contour.

Figure 2(a) shows initial penetration of the stratified layer by the plume cap. As the plume rises through the stratified layer, its upward acceleration decreases as the relative buoyancy between the plume and the surrounding environment decreases. Once the environmental buoyancy exceeds that of the plume, the plume decelerates. Eventually, the rising fluid reverses direction, or 'overturns', and begins to subside from the maximum penetration height z_{max} (figure 2b). As plume fluid subsides, its buoyancy relative to the surrounding environment increases until reaching the level of neutral buoyancy z_n where the plume fluid forms a radially spreading intrusion – see figure 2(c). The dynamics observed in the simulation agrees qualitatively with studies of similar set-ups in the literature, for example the experiments detailed in Ansong & Sutherland (2010) with an identical set-up and similar physical parameters.

The evolution of the maximum height of the plume cap during penetration and the subsequent quasi-steady state is visualised as a time series of tracer concentration on the plume centreline in figure 3. As has been noted in the literature, the maximum height of the plume tends to oscillate around a quasi-steady state height z_{ss} (Turner 1966) but, to our knowledge, the mechanism setting the frequency of this oscillation (often referred to as 'plume bobbing') is not well understood (e.g. Ansong & Sutherland 2010). In the simulation considered here, the quasi-steady state height z_{ss} is close to the maximum penetration height z_{max} and the oscillation is weak. For convenience, we will use z_{max} to refer to the maximum height of the plume. The maximum penetration height z_{max} determines the maximum height at which plume fluid can mix with the environment (Ansong, Kyba & Sutherland 2008), meaning the initial buoyancy at the maximum penetration height, $b = z_{max}$, represents a plausible constraint on the maximum buoyancy accessible for mixing with the plume. However, this constraint can occasionally be exceeded when plume fluid subsiding from the plume cap pulls very buoyant environmental fluid downwards (see figure 2(b) to the left of the plume cap). Here we
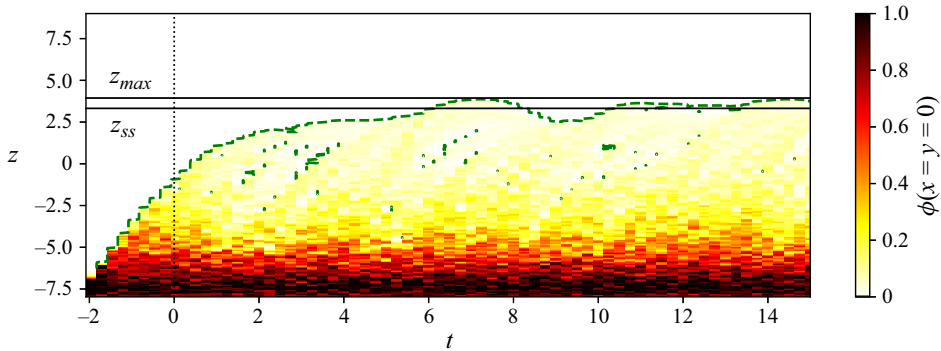
Figure 3. Time series of the tracer concentration $\phi(0, 0, z, t)$ in the z–t plane at the centreline of the computational domain $x = y = 0$. The green dashed contour denotes the plume threshold $\phi = \phi_{min}$, i.e. where ϕ is 1 % of its value on the plume centreline. The maximum penetration height z_{max} and the quasi-steady state height z_{ss} are marked.

find $z_{max} = 3.94$ which agrees with experimental estimates of the maximum penetration height in the literature, e.g. $z_{max} \approx 3.8$ for a plume with a round source (List 1982).

Internal gravity waves across a range of frequencies are generated during the penetration process. These waves are visible as small amplitude, long wavelength undulations in the buoyancy contours above $z \approx 4$ in figure 2(*c*). Any influence of internal gravity waves on mixing in this flow will be present in the analyses, but it is beyond the scope of this paper to determine the particular contribution of these waves to mixing.

In the uniform layer, the buoyancy and tracer evolve identically up to a linear factor, i.e. the undiluted plume fluid entering the stratified layer has a linear relationship between b and ϕ at each point. This follows from the self-similarity of the buoyancy and tracer concentration profiles in the steady state plume that penetrates the stratified layer (see Appendix B, figure 18). The radial profiles for b and ϕ are both Gaussian with the same width but different amplitudes, hence $b \propto \phi$. After penetrating the stratified layer, plume fluid with non-zero buoyancy and tracer concentration mixes with tracer-less environmental fluid and hence the buoyancy and tracer evolve differently. This effect can be quantified using a tracer probability density function (p.d.f.) in buoyancy coordinates $\tilde{\phi}(b; t)$. The p.d.f. is calculated within the stratified layer only. The value of the p.d.f. $\tilde{\phi}(b; t)$ is calculated as the total tracer with buoyancy within a range b to $b + \mathrm{d}b$ in the stratified layer, normalised by the total tracer in the stratified layer $\phi_T(t) = \sum_V \phi(\boldsymbol{x}, t) \Delta V$, where V is the stratified layer and ΔV is the grid-cell volume. The definition of $\tilde{\phi}$ is such that $\sum_B \tilde{\phi}(B; t) = 1$.

Figure 4 shows $\tilde{\phi}(b; t)$ in the stratified layer at fixed time intervals post-penetration. The total tracer in the stratified layer $\phi_T(t)$ is shown inset. The approximately linear increase in ϕ_T with time suggests a relatively uniform input of tracer to the stratified layer, carried by the penetrating plume. Owing to the self-similar nature of the penetrating plume, we expect the tracer that enters the stratified layer to have a fixed p.d.f. (with some small variation). This pre-penetration p.d.f. $\tilde{\phi}_0$ can be estimated using a domain V chosen as the pre-penetration region shown in figure 1. This region is a thin layer with (non-dimensional) depth $1/2$ below the bottom of the stratified layer. The pre-penetration p.d.f., shown as a black dashed line in figure 4, represents the tracer p.d.f. in the plume just before it penetrates the stratified layer. Without mixing, $\tilde{\phi}$ in the stratified layer would match the
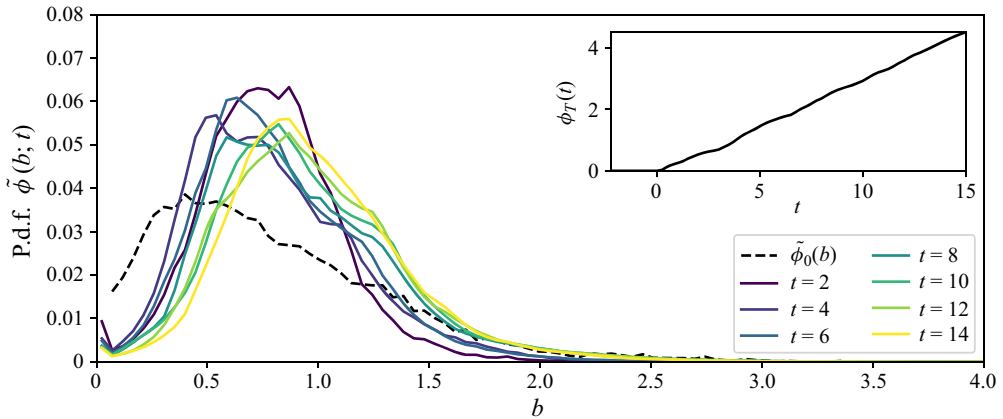
Figure 4. Probability density function $\tilde{\phi}(b, t)$ of tracer as a function of buoyancy b in the stratified layer at fixed time intervals post-penetration shown as coloured lines. The black dashed line shows the time-averaged pre-penetration p.d.f. $\tilde{\phi}_0(b)$, calculated with V chosen as the pre-penetration region indicated in figure 1 and time averaged. The pre-penetration p.d.f. $\tilde{\phi}_0(b)$ shows the tracer-buoyancy relationship within the plume prior to penetrating the stratified layer. Differences between $\tilde{\phi}_0$ and $\tilde{\phi}(b, t)$ represent the effect of mixing. Total tracer in the stratified layer $\phi_T(t)$ shown inset.

pre-penetration p.d.f. Mixing during the penetration process manifests as changes in the tracer p.d.f. when compared with the pre-penetration p.d.f.

Evolution of the post-penetration p.d.f. and changes compared with the pre-penetration tracer p.d.f. highlight two mixing processes during penetration: mixing within the plume during penetration, and mixing between the plume and environment. Where plume fluid carries a large tracer concentration and mixes with the more buoyant surroundings, the positive tail of the tracer p.d.f. increases. This is particularly evident after $t = 6.75$ when the plume has reached $z_{max} = 3.94$, at which point very large values of buoyancy in the environment become accessible and large tracer concentrations at the centre of the plume are exposed to the environment as plume fluid overturns. At the edges of the plume where tracer concentration is smallest, mixing with the environment again moves tracer from lower to higher values of buoyancy and therefore the p.d.f. decreases where b is small. This effect is supplemented by mixing within the plume, which acts to homogenise the large tracer concentration and buoyancy at the centre of the plume with the lower tracer concentration and buoyancy at the edge of the plume. This acts to narrow the p.d.f. and hence decrease the p.d.f. at large and small values of buoyancy but the effect is only evident before the plume reaches z_{max} at $t = 6.75$ and accesses much larger values of buoyancy. At late times, most tracer lies in the spreading intrusion at the neutral buoyancy height z_n, which coincides with the peak in the tracer p.d.f.

The buoyancy range of the tracer p.d.f. is determined by the maximum penetration height of the plume as well as the rapidity of the mixing between the plume and environment occurring in the plume cap. If fluid quickly reaches z_{max} and subsides before substantial mixing with the environment occurs, only small amounts of the more buoyant environment are entrained and therefore the increase in the p.d.f. at large values of buoyancy is modest compared with a scenario where plume fluid stalls during overturning and significant mixing with the environment occurs. In figure 4, the tracer p.d.f. extent is $b \approx 3$ whilst the environmental buoyancy at z_{max} is approximately $b|_{z_{max}} \approx 3.94$. This suggests the mixing time scale is slow compared with the dynamical time scale, i.e. mixing between the largest tracer concentrations first exposed during overturning and

997 A48-8

the environment is slow and continues during subsidence, where the buoyancy of the environment decreases.

The tracer p.d.f. hints at competing effects of mixing within the plume and between the plume and the environment. Crucially, the buoyancy and tracer fields are mixed in different ways owing to the linearly increasing buoyancy and vanishing tracer concentration in the linearly stratified environment. Whilst changes in the tracer p.d.f. considered here demonstrate the overall effect on the relation between tracer and buoyancy, it is difficult to extract information on the intensity of mixing between plume and environmental fluid and the specific buoyancy and tracer characteristics of the fluid parcels that mix. Furthermore, the tracer p.d.f. $\tilde{\phi}(b; t)$ does not give information on the volume of fluid parcels at a given buoyancy; a peak in the tracer p.d.f. may represent relatively few fluid parcels carrying large tracer concentrations or many fluid parcels carrying small amounts of tracer. The distinction is important, since the former can result in stronger gradients upon which diffusion acts and therefore more effective diapycnal transport of tracer.

4. Buoyancy-tracer volume distribution

The probability distributions of tracer concentration discussed in §3 isolate the irreversible transport that results from turbulent mixing. The turbulent mixing of fluid parcels can be considered a two-step process (e.g. Davies Wykes & Dalziel 2014), composed of stirring and molecular diffusion. Whilst stirring strengthens tracer gradients across buoyancy surfaces, it is – in principle – a reversible process. However, molecular diffusion results in irreversible changes to the buoyancy and tracer characteristics of fluid parcels and hence changes the tracer distribution.

Here, we use the distribution of volume in buoyancy-tracer space to diagnose mixing in the stratified layer. That is, we map from three-dimensional physical space to a two-dimensional phase space by using the buoyancy and tracer concentration fields to quantify the volume of plume fluid in the stratified layer with each value of b and ϕ. The total physical volume of plume fluid represented in the distribution changes in time and we do not normalise the distribution to form a p.d.f. Omitting this normalisation simplifies the interpretation of the distribution and its governing equation. The buoyancy-tracer volume distribution formalism presented here builds on previous density–tracer joint p.d.f. formulations presented by Plumb (2007) and Penney *et al.* (2020).

4.1. *Definition and properties*

We define the volume distribution $W(B, \Phi; t)$ in buoyancy-tracer space such that the volume of fluid in a fixed volume V with $B < b(\boldsymbol{x}, t) < B + \mathrm{d}B$ and $\Phi < \phi(\boldsymbol{x}, t) < \Phi + \mathrm{d}\Phi$ is given by $W(B, \Phi; t) \, \mathrm{d}B \, \mathrm{d}\Phi$. This may be defined as

$$W(B, \Phi; t) = \int_V \delta(b(\boldsymbol{x}, t) - B)\delta(\phi(\boldsymbol{x}, t) - \Phi) \, \mathrm{d}V, \tag{4.1}$$

where $\delta(\cdot)$ is the Dirac delta function with the inverse dimension of its argument. Henceforth, we choose the volume V to be the stratified layer. An evolution equation for W can be obtained using the governing equations for b and ϕ. See Appendix C for a full derivation. We have

$$\frac{\partial W}{\partial t} = -\boldsymbol{\nabla}_{(B, \Phi)} \cdot \boldsymbol{F} + S, \tag{4.2}$$

where $\boldsymbol{F}(B, \Phi; t)$ is the mixing flux distribution and $S(B, \Phi; t)$ is the source distribution. The mixing flux distribution $\boldsymbol{F}$ is a vector in buoyancy-tracer space with components

formed from the volume-weighted average of the non-advective terms $\dot{b}$ and $\dot{\phi}$ in (2.3) and (2.4) respectively, representing the flux of W in buoyancy-tracer space due to mixing and is defined as

$$\boldsymbol{F}(B, \Phi; t) = (F_b, F_\phi) = \int_V (\dot{b}, \dot{\phi}) \delta(b(\boldsymbol{x}, t) - B) \delta(\phi(\boldsymbol{x}, t) - \Phi) \, \mathrm{d}V, \quad (4.3)$$

where $\dot{b} = (RePr)^{-1} \nabla^2 b - \nabla \cdot \boldsymbol{\lambda}_b$ and $\dot{\phi} = (RePr)^{-1} \nabla^2 \phi - \nabla \cdot \boldsymbol{\lambda}_\phi$. Note that the plume forcing terms f_b and f_ϕ are excluded from $\dot{b}$ and $\dot{\phi}$ since the forcing vanishes in the stratified layer. The source distribution S represents a source or sink of W due to boundary fluxes across ∂V

$$S(B, \Phi; t) = \int_{\partial V} \boldsymbol{u} \cdot \boldsymbol{n} \, \delta(b(\boldsymbol{x}, t) - B) \delta(\phi(\boldsymbol{x}, t) - \Phi) \, \mathrm{d}A, \quad (4.4)$$

where $\boldsymbol{u}$ is the velocity in physical space and $\boldsymbol{n}$ is the inward normal on the boundary ∂V of V. Since we are considering a flow upwards into V, $\boldsymbol{u} \cdot \boldsymbol{n}$ is positive and S acts as a source of W. Note that whilst S represents the effect of fluxes across the boundary ∂V in physical space, it is distributed in buoyancy-tracer space. Note that (4.2) contains no terms in which advection plays an explicit role except for the source term – which captures advection through the domain boundary – representing the fact that W remains unchanged under advection within the domain.

Turbulent mixing redistributes volume in buoyancy-tracer space, which results in changes to W via the mixing flux term $-\nabla_{(B,\Phi)} \cdot \boldsymbol{F}$. The change in W at a point (B, Φ) in buoyancy-tracer space as a result of turbulent mixing up to time t is therefore

$$M(B, \Phi; t) = -\int_0^t \nabla_{(B,\Phi)} \cdot \boldsymbol{F}(B, \Phi; t') \, \mathrm{d}t' = W(B, \Phi; t) - \int_0^t S(B, \Phi; t') \, \mathrm{d}t', \quad (4.5)$$

such that $M(B, \Phi; t) \, \mathrm{d}B \, \mathrm{d}\Phi$ is the change in volume of fluid with $B < b(\boldsymbol{x}, t) < B + \mathrm{d}B$ and $\Phi < \phi(\boldsymbol{x}, t) < \Phi + \mathrm{d}\Phi$ up to time t due to mixing. Therefore M represents the integrated effect of the mixing flux $\boldsymbol{F}$ and we refer to M as the net mixing effect distribution. The second equality in (4.5) follows from time integrating (4.2) and noting that $W(B, \Phi; t = 0) = 0$ since there is no tracer in the initial stratified layer. Hence, M can be interpreted as a cumulative measure of the changes to W relative to the time-integrated source distribution, i.e. the changes in the volume distribution that arise solely from mixing. The final term in (4.5), which we refer to as the cumulative source distribution, represents the volume of fluid with buoyancy $B < b < B + \mathrm{d}B$ and tracer concentration $\Phi < \phi < \Phi + \mathrm{d}\Phi$ that has entered the stratified layer up to time t. The volume distribution $W \geqslant 0$ and the cumulative source distribution is also positive assuming there is a flow into V only. However, M can be positive or negative depending on the relative sizes of the volume distribution and the cumulative source distribution.

The net mixing effect distribution $M(B, \Phi; t)$ is positive in buoyancy-tracer space where more volume is present at time t than has entered the stratified layer up to time t, i.e. there is a net gain in the volume of fluid with buoyancy B and tracer concentration Φ due to mixing. Correspondingly, $M(B, \Phi; t)$ is negative where more volume has entered the stratified layer up to time t with buoyancy B and tracer concentration Φ than currently exists at time t, i.e. there is a net loss in the volume of fluid with buoyancy B and tracer concentration Φ due to mixing. The value of M therefore indicates the transfer of volume within W due to mixing; fluid leaves regions of buoyancy-tracer space with $M < 0$ and enters regions with $M > 0$.

To summarise, the distributions $W, S, \boldsymbol{F}$ and M together describe the flow in terms of its effect on buoyancy-tracer space. The volume distribution W is an instantaneous

representation of the amount of fluid within the stratified layer with given ranges of values of buoyancy and tracer concentration. Large values of W indicate large volumes of fluid with a narrow range of b and ϕ, though the fluid parcels corresponding to this range are not necessarily co-located in physical space. The source distribution S represents the volume distribution of fluid that enters the stratified layer from the uniform layer. In the absence of mixing, W would be equivalent to the time integral of S. The mixing flux distribution F represents the redistribution of fluid in buoyancy-tracer space due to mixing. The net mixing flux distribution M captures the change in W relative to time-integrated S via F and indicates where there is accumulation or loss of volume due to mixing.

4.2. *Idealised example*

The effect of an idealised turbulent mixing event on buoyancy-tracer space is illustrated in figure 5. The top row shows the volume distribution containing three initial fluid parcels (blue points) which have entered the stratified layer. As turbulent stirring brings these fluid parcels together, another fluid parcel (green point) enters the domain and all four fluid parcels mix. The resulting mixed fluid parcel (red point) is a volume-weighted average of the fluid parcels involved in the mixing event. The bottom row shows the distributions after the mixing event. The volume distribution W is non-zero (and positive) only where the final mixture lies in buoyancy-tracer space and the direction of the mixing flux vectors F indicates the redistribution of volume. The cumulative source distribution $\int_0^t S \, \mathrm{d}t'$ is positive at the values of b and ϕ where the fluid parcels entered the domain and vanishes elsewhere. The net mixing effect distribution M is negative at these points, as volume has been lost, and positive where the mixed fluid parcel lies as volume has been gained. These principles can be used to understand the mixing processes in the physical flow that result in changes in the distribution in buoyancy-tracer space. Whilst it is not possible to isolate distinct fluid parcels that are mixing at any one time, we can identify physical regions of the flow that are subject to turbulent mixing and isolate the corresponding regions of buoyancy-tracer space.

Turbulent mixing acts to homogenise the buoyancy and tracer concentration of fluid parcels. Provided the molecular diffusivities of buoyancy and tracer are equal, a mixture of two fluid parcels lies on a line between the two parcels in buoyancy-tracer space (Penney *et al.* 2020). Therefore, as the buoyancy-tracer volume distribution W evolves, it is constrained to lie within its own past convex envelope, i.e. the smallest convex set that contains all non-zero points of the distribution. As illustrated in figure 5, this convex envelope must include fluid that enters the domain during the mixing process. The convex envelope of the initial volume distribution is indicated by the dotted envelope and the dashed envelope indicates the convex envelope including newly arriving fluid parcels. We emphasise that the final mixed fluid parcel is contained within the convex envelope of initial and newly arriving fluid, but not necessarily within the convex envelope of the initial fluid only. The principle of homogenising fluid parcels illustrated in figure 5 can be generalised to continuous mixing of fluid in a flow, in which case the convex envelope constraint applies to the volume distribution as a whole. This implies that in the absence of sources the convex envelope reduces over time and converges towards some compact distribution (Penney *et al.* 2020). In the set-up we consider, fluid entering the stratified layer causes the extremes of the distribution to persist, whilst turbulent mixing acts to continuously shift the buoyancy-tracer characteristics of fluid towards an accumulation region in buoyancy-tracer space.

(*a*)

● Initial fluid parcels
⋯⋯ Initial convex envelope

● Arriving fluid parcel

‑‑‑ Initial + newly arriving fluid convex envelope

● Final mixture

⟶ Flux **F** of *W*

(*b*)

Final distributions

⊕ Positive values   ⊖ Negative values

Volume distribution *W* & mixing flux distribution **F**

Cumulative source distribution $\int_0^t S \, dt'$
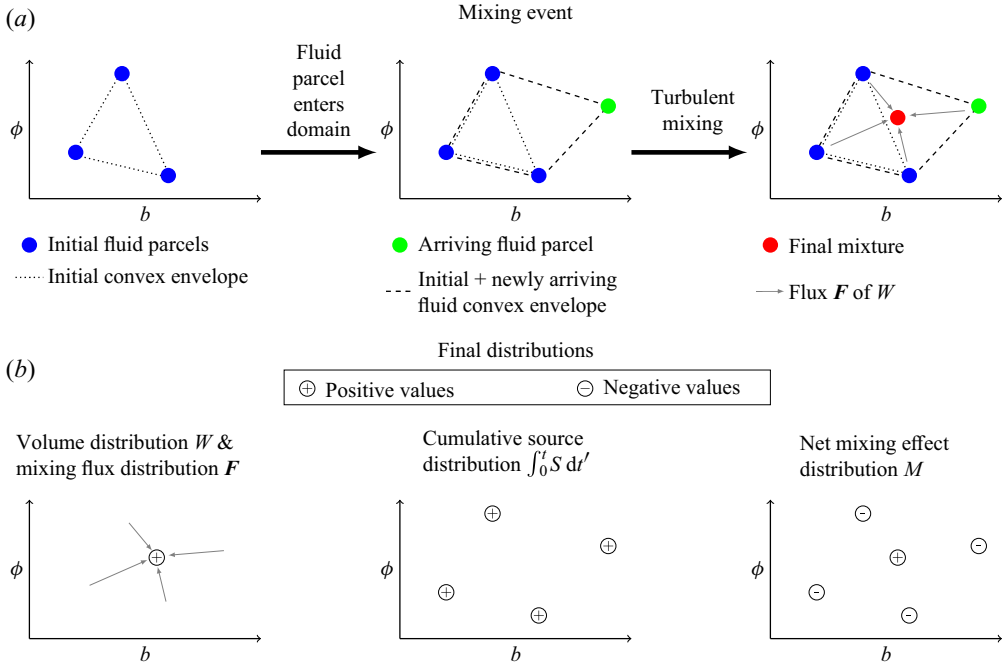
Net mixing effect distribution *M*

Figure 5. Schematic diagram of the effect in buoyancy-tracer space of an idealised turbulent mixing event between a set of discrete fluid parcels that have entered the stratified layer and a fluid parcel that later enters the stratified layer. The top row illustrates the convex envelope property of the volume distribution *W*, which implies that a mixture of a set of fluid parcels lies within the smallest envelope that contains the distribution of the fluid parcels that are mixed together. The distributions *W*, $\int S \, dt$ and *M* following the idealised mixing event are shown on the bottom row. Positive (arbitrary) values of each distribution are indicated by a circled $+$, negative (arbitrary) values are indicated by a circled $-$. The mixing flux distribution vectors **F** are indicated by grey arrows.

4.3. *Numerical implementation*

To examine the numerical simulation detailed in §§ 2 and 3, we use a discrete formulation of the buoyancy-tracer volume distribution introduced in § 4.1. We choose the domain *V* to be tracer-containing plume fluid within the stratified layer. The stratified layer initially corresponds to the volume $z \geqslant 0$. However, the plume can perturb the bottom of the stratified layer slightly below $z = 0$. We therefore define the domain as the region where $-1 \leqslant z \leqslant L_z$, $\phi > \phi_{min}$, and $b > 0$. As a consequence, the 'reservoir' of environmental fluid where $\phi = 0$ is excluded. In interpreting results, we therefore consider the boundary $\phi = \phi_{min}$ as a source where volume can enter the distribution from the environment. The entrainment of environmental fluid across this boundary in buoyancy-tracer space into the volume distribution is discussed in § 4.7 and illustrated in figure 7.

The buoyancy and tracer domains are subdivided into N_b and N_ϕ equally sized bins of size $\delta B = (b_{max} - b_{min})/N_b$ and $\delta \Phi = (\phi_{max} - \phi_{min})/N_\phi$ respectively. We choose $b_{min} = 0$ and $b_{max} = 4$ since the largest accessible buoyancy is related to the maximum penetration height (Ansong *et al.* 2008) which is experimentally predicted to be $z_{max} \leqslant 4$ (List 1982). To accommodate fluctuations in tracer concentration, we choose ϕ_{max} to be larger than the tracer concentration on the plume centreline $2\phi_m(0)$ at penetration height $z = 0$ using the profile predicted by the Morton *et al.* (1956) plume equations, $\phi_m(z)$,

997 A48-12

defined in (A5) (see Appendix A for details). We use $\phi_{min} = 10^{-2}$, consistent with the plume threshold introduced in § 3. Henceforth we use $N_b = N_\phi = 256$.

Denoting the centre of a given bin as (B_i, Φ_j), the associated value of the volume distribution is computed as

$$W_{ij}(t) = \sum_V I_{ij}(\mathbf{x}, t) \Delta x \Delta y \Delta z, \tag{4.6}$$

where the sum is over all grid points within the domain V, Δx, Δy, Δz are the grid-cell widths and the indicator $I_{ij}(\mathbf{x}, t)$ is defined as

$$I_{ij}(\mathbf{x}, t) = \begin{cases} 1 & \left(b(\mathbf{x}, t) - B_i, \phi(\mathbf{x}, t) - \Phi_j\right) \in \left(-\tfrac{1}{2}\delta B, \tfrac{1}{2}\delta B\right] \times \left(-\tfrac{1}{2}\delta\Phi, \tfrac{1}{2}\delta\Phi\right], \\ 0 & \text{otherwise.} \end{cases} \tag{4.7}$$

The value of $W_{ij}(t)$ therefore represents the total volume within V where the buoyancy lies within $\delta B/2$ of B_i and the tracer concentration lies within $\delta\Phi/2$ of Φ_j. Note that in the continuous formulation, the volume distribution $W(B, \Phi; t)$ defined by (4.1) must be integrated over B and Φ to yield a volume, whilst $W_{ij}(t)$ itself has dimensions of volume and need only be summed over i and j. The continuous and discrete formulations coincide in the limit $\delta B, \delta\Phi \to 0$, such that

$$\lim_{\delta B, \delta\Phi \to 0} \frac{W_{ij}(t)}{\delta B \delta\Phi} = W(B_i, \Phi_j; t). \tag{4.8}$$

The equivalence (4.8) also applies to the discrete mixing flux distribution $F_{ij}(t)$, the discrete source distribution $S_{ij}(t)$ and the discrete net mixing effect distribution $M_{ij}(t)$ defined by

$$\mathbf{F}_{ij}(t) = (F_{ij}^b(t), F_{ij}^\phi(t)) = \sum_V I_{ij}(\mathbf{x}, t)(\dot{b}, \dot{\phi}) \Delta x \Delta y \Delta z, \tag{4.9}$$

$$S_{ij}(t) = \sum_{\partial V} I_{ij}(\mathbf{x}|_{z=-1}, t) w(\mathbf{x}|_{z=-1}, t) \Delta x \Delta y, \tag{4.10}$$

$$M_{ij}(t) = W_{ij}(t) - \sum_{t'} S_{ij}(t') \Delta t', \tag{4.11}$$

where $\Delta t'$ is the simulation time step. In (4.9), $\dot{b}$ and $\dot{\phi}$ are the non-advective terms in the scalar evolution equations (2.3), (2.4) of b, ϕ respectively, as defined in § 4.1. In (4.10) we have used the fact that $\mathbf{n} = \hat{\mathbf{k}}$ on the bottom boundary of the domain V.

4.4. *Results*

The discrete formulation of the distributions given in § 4.3 provides an approximation to the continuous formulation and is presented in all figures shown below. However, the interpretation is the same as the continuous formulation and we will refer to the continuous formulation in all discussions. Quantities derived from the distributions are given in both continuous and discrete forms for completeness. In defining the discrete and continuous formulations we use the arguments B and Φ, which represent values of buoyancy and tracer concentration respectively. We treat W, F, S and M as functions of b and ϕ to aid clarity, e.g. $W(b, \phi; t)$, with the interpretation that b and ϕ represent values of buoyancy and tracer concentration found in the flow in the same way as B and Φ in §§ 4.1 and 4.3.
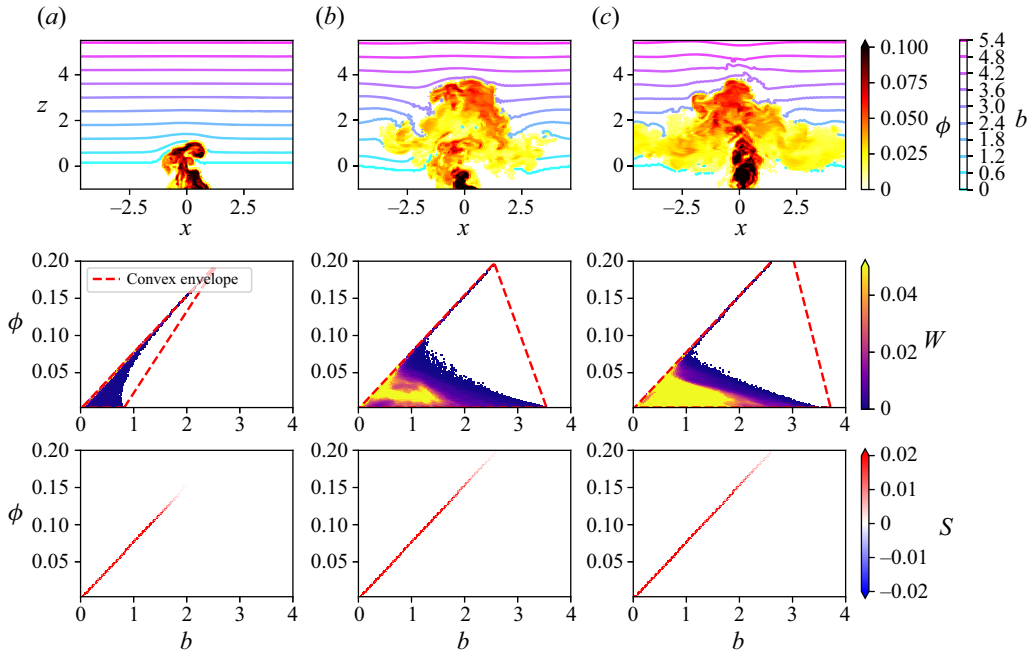
Figure 6. Three instantaneous snapshots showing the evolution of the buoyancy-tracer volume distribution $W(b, \phi; t)$ (middle) and source distribution $S(b, \phi; t)$ (bottom) at non-dimensional times $t = 1, 6.75, 14$ corresponding with figure 2. The convex envelope of the volume distribution W at time t is shown as a red dashed line in the middle panel. To aid interpretation, we also show $x - z$ cross-sections of the tracer concentration and buoyancy contours, as in figure 3 (top).

Figure 6 shows the buoyancy-tracer volume distribution $W(b, \phi; t)$ (middle row), the source distribution $S(b, \phi; t)$ (bottom row), and $x - z$ cross-sections of the tracer concentration field and buoyancy contours (top row). These results are shown at three snapshots corresponding with stages of the flow evolution as in figure 2. The distributions are shown only where non-zero, i.e. regions of buoyancy-tracer space which are not coloured indicate that there is no fluid with buoyancy and tracer concentration in that range. In each snapshot of W, the red dashed lines show the convex envelope that constrains the evolution of the volume distribution. As seen in the figure, the source distribution lies within the convex envelope of $W(b, \phi; t)$. Furthermore, as the plume rises and accesses more buoyant fluid in the surrounding environment, the convex envelope is extended along the $\phi = 0$ axis as new environmental fluid becomes accessible via mixing.

The results shown in figure 6 illustrate how the volume distribution captures the dynamics and mixing processes at each stage of the flow evolution. We first note that the source distribution $S(b, \phi; t)$ takes positive values only, since there is only a flow into the stratified layer. Furthermore, S is non-zero only on a line through the origin as expected from the linear relationship between b and ϕ in the rising plume. We refer to this as the source line. Given that the convex envelope of a set of points on a line segment is the same line segment, mixing of undiluted plume fluid within the plume only redistributes fluid on the source line. When undiluted plume fluid mixes with the surrounding environment, it is moved away from the source line. This offers a clear distinction between undiluted and mixed plume fluid, as illustrated schematically in figure 7. In the buoyancy-tracer volume distribution W shown on the middle row of figure 6, fluid appearing away from the source line therefore represents a mixture of plume and environmental fluid. Further information
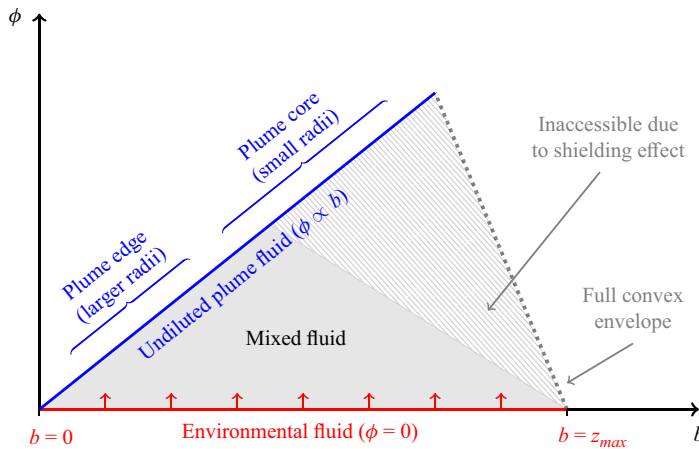
Figure 7. Schematic diagram illustrating the correspondence between regions in physical space and regions in buoyancy-tracer space. Environmental fluid is represented by the b axis where $\phi = 0$ (red), between the bottom of the stratified layer where $b = 0$ and the maximum penetration height where $b = z_{max}$. Undiluted plume fluid lies on the source line where $\phi \propto b$ (blue), with large b and ϕ in the core of the plume and small b and ϕ towards the edges. Mixed fluid lies between these two lines, within their convex envelope (dotted grey). Some regions of the convex envelope (hatched area) are inaccessible due to the shielding effect of the plume edge (where ϕ is non-zero but small) and the intrusion surrounding the rising plume. Volume entering the distribution due to entrainment of environmental fluid is indicated by the red arrows.

on the regions of the undiluted plume that mix with the environment is gained by noting that, owing to the Gaussian profiles of the plume pre-penetration, b and ϕ are larger near the centreline of the plume and smaller towards the edge of the plume (see figure 6c). Hence fluid near the 'plume edge' lies nearest the origin on the source line whilst fluid in the 'plume core' lies at the extreme end of the source line.

Figure 6(a) shows the plume shortly after penetrating the stratified layer and before reaching its maximum penetration height. At this stage, only the edges of the plume are exposed to the environment in the lower part of the stratified layer which has a relatively small buoyancy. We therefore find volume appearing in a small region of the convex envelope closest to the origin in buoyancy-tracer space. In figure 6(b), the plume has reached its maximum penetration height and undiluted plume fluid in the plume core, which has until this stage been shielded from the environment by the edges of the plume, overturns and becomes exposed to environmental fluid near z_{max} with relatively large buoyancy. The volume distribution at this time covers a wider range of b and ϕ as environmental fluid with a large range of buoyancy is able to mix with much of the undiluted plume fluid lying on the source line. However, note that we do not see mixing between the extreme end of the source line and the environment (see hatched region in figure 7). As undiluted plume fluid in the core of the plume rises, turbulent mixing acts to homogenise the buoyancy and tracer concentration within the source distribution, reducing the largest values of b and ϕ near the centreline of the plume. Hence, when this fluid is first exposed to the environment in the plume cap, it lies closer to the middle of the source line. We refer to this as the shielding effect. Note that the large values of b and ϕ on the source line appear to persist, and may increase, due to new undiluted plume fluid entering the stratified layer.

Figure 6(c) shows the quasi-steady state plume where there is a continuous input of undiluted plume fluid along the source line $\phi \propto b$, mixing between the plume and

C.W. Powell, P.H. Haynes and J.R. Taylor

environment up to values of buoyancy corresponding to heights near z_{max} and an
accumulation of fluid at lower values of buoyancy and tracer concentration corresponding
to the radially spreading intrusion. The intrusion dominates the total volume of the
plume at late times and is represented by the region of large W at intermediate values
of buoyancy and tracer concentration. Note that the intrusion enhances the shielding effect
by preventing undiluted plume fluid from accessing the environment before reaching the
plume cap.

4.5. *Quasi-steady state*

In this flow, quasi-steady state refers to the long-term behaviour established once an
intrusion has formed. In this state, undiluted plume fluid continuously arrives in the
stratified layer, mixes with the environment and accumulates in the intrusion. This means
that in quasi-steady state the volume of undiluted plume fluid in the stratified layer
remains roughly constant whilst the full plume volume (i.e. the sum of the rising undiluted
plume, plume cap and intrusion), and in particular the volume of the intrusion, increases
monotonically.

To quantitatively identify the time at which quasi-steady state (QSS) starts, first we
define the source line more generally as the region where the cumulative source volume
is positive, $\mathcal{S} = \{(b, \phi) | \int_0^t S(b, \phi; t')\, dt' > 0\}$. Next, we can define the volume associated
with any region $\mathcal{R}$ of buoyancy-tracer space at time t as

$$V(\mathcal{R}; t) = \int_{\mathcal{R}} W(b, \phi; t)\, db\, d\phi = \sum_{\mathcal{R}} W_{ij}(t). \qquad (4.12)$$

We expect that in QSS $dV(\mathcal{S})/dt \approx 0$. However, 'plume bobbing' (i.e. the up-and-down
motion of the plume cap noted in § 3) results in some variation of the volume of the source
line. The quasi-steady volume of undiluted plume fluid $V(\mathcal{S})$ can also gradually increase
over time owing to the shielding effect. We therefore introduce an alternative constraint
for identifying QSS which utilises the net mixing effect distribution M. As illustrated in
figure 7, the source line represents undiluted plume fluid arriving in the stratified layer,
which introduces volume into the distribution that is eventually mixed away from the
source line. In the transient penetration stage, turbulent mixing redistributes fluid on the
source line before mixing with the environment. Hence, there is some accumulation on
parts of the source line and $M > 0$. However, once the plume reaches QSS and mixing
with the environment continuously removes volume from the source line, M must become
negative. Away from the source line, S vanishes so M is necessarily positive according
to (4.5). We define the region $\mathcal{U} = \{(b, \phi)|M(b, \phi; t) < 0\}$ and identify QSS as the time
when the volume associated with $\mathcal{U}$, $V(\mathcal{U})$, is within 10 % of the volume of the source line
$V(\mathcal{S})$. These volumes and the time we identify as the start of QSS, $t_{QSS} \approx 3.5$, are shown
in figure 8(a).

4.6. *Source, transport and accumulation regions*

We now restrict attention to QSS $t > t_{QSS}$, i.e. ignoring any transient dynamics during
initial penetration. Here, we discuss the results for M and show that this distribution can
be used to partition plume fluid into three classes which identify coherent regions of the
plume.

Figure 9 shows the net mixing effect distribution in both physical and buoyancy-tracer
space at $t = 14$, with the mixing flux distribution vectors F overlaid in buoyancy-tracer

997 A48-16

C.W. Powell, P.H. Haynes and J.R. Taylor

environment up to values of buoyancy corresponding to heights near z_{max} and an accumulation of fluid at lower values of buoyancy and tracer concentration corresponding to the radially spreading intrusion. The intrusion dominates the total volume of the plume at late times and is represented by the region of large W at intermediate values of buoyancy and tracer concentration. Note that the intrusion enhances the shielding effect by preventing undiluted plume fluid from accessing the environment before reaching the plume cap.

4.5. *Quasi-steady state*

In this flow, quasi-steady state refers to the long-term behaviour established once an intrusion has formed. In this state, undiluted plume fluid continuously arrives in the stratified layer, mixes with the environment and accumulates in the intrusion. This means that in quasi-steady state the volume of undiluted plume fluid in the stratified layer remains roughly constant whilst the full plume volume (i.e. the sum of the rising undiluted plume, plume cap and intrusion), and in particular the volume of the intrusion, increases monotonically.

To quantitatively identify the time at which quasi-steady state (QSS) starts, first we define the source line more generally as the region where the cumulative source volume is positive, $\mathcal{S} = \{(b, \phi) | \int_0^t S(b, \phi; t')\, dt' > 0\}$. Next, we can define the volume associated with any region $\mathcal{R}$ of buoyancy-tracer space at time t as

$$V(\mathcal{R}; t) = \int_{\mathcal{R}} W(b, \phi; t)\, db\, d\phi = \sum_{\mathcal{R}} W_{ij}(t). \qquad (4.12)$$

We expect that in QSS $dV(\mathcal{S})/dt \approx 0$. However, 'plume bobbing' (i.e. the up-and-down motion of the plume cap noted in § 3) results in some variation of the volume of the source line. The quasi-steady volume of undiluted plume fluid $V(\mathcal{S})$ can also gradually increase over time owing to the shielding effect. We therefore introduce an alternative constraint for identifying QSS which utilises the net mixing effect distribution M. As illustrated in figure 7, the source line represents undiluted plume fluid arriving in the stratified layer, which introduces volume into the distribution that is eventually mixed away from the source line. In the transient penetration stage, turbulent mixing redistributes fluid on the source line before mixing with the environment. Hence, there is some accumulation on parts of the source line and $M > 0$. However, once the plume reaches QSS and mixing with the environment continuously removes volume from the source line, M must become negative. Away from the source line, S vanishes so M is necessarily positive according to (4.5). We define the region $\mathcal{U} = \{(b, \phi)|M(b, \phi; t) < 0\}$ and identify QSS as the time when the volume associated with $\mathcal{U}$, $V(\mathcal{U})$, is within 10 % of the volume of the source line $V(\mathcal{S})$. These volumes and the time we identify as the start of QSS, $t_{QSS} \approx 3.5$, are shown in figure 8(a).

4.6. *Source, transport and accumulation regions*

We now restrict attention to QSS $t > t_{QSS}$, i.e. ignoring any transient dynamics during initial penetration. Here, we discuss the results for M and show that this distribution can be used to partition plume fluid into three classes which identify coherent regions of the plume.

Figure 9 shows the net mixing effect distribution in both physical and buoyancy-tracer space at $t = 14$, with the mixing flux distribution vectors F overlaid in buoyancy-tracer

997 A48-16

https://doi.org/10.1017/jfm.2024.662 Published online by Cambridge University Press

Figure 8. (*a*) Volume of the source line $\mathcal{S} = \{\int_0^t S(b, \phi; t') \, dt' > 0\}$ (dashed line) and the region $\mathcal{U} = \{M(b, \phi; t) < 0\}$ (solid line). The start of QSS (vertical dotted line) is identified as the time when these volumes agree to within 10 %. (*b*) Decomposition of the full plume volume into undiluted plume fluid, plume cap and intrusion (solid coloured lines) using the partitioning introduced in § 4.6. The total plume input volume up to time t (black dashed line) is shown for reference.

space. The distribution is represented in physical space by using the buoyancy and tracer concentration to map between buoyancy-tracer space and physical space, i.e. we plot $M(b(\boldsymbol{x}, t), \phi(\boldsymbol{x}, t); t)$. To avoid confusion between regions of buoyancy-tracer space and the corresponding fluid in physical space, we refer to the former as regions and the latter as classes of fluid. Recall that the net mixing effect distribution, M, quantifies the integrated effect of the mixing flux distribution, $\boldsymbol{F}$, or, equivalently, the volume difference between the volume distribution and the cumulative source distribution, representing the volume change due to mixing. As expected, we find $M < 0$ on the source line where undiluted plume fluid is continuously supplied before being mixed away into the $M > 0$ region. Environmental fluid is entrained into the plume via mixing and accumulates in the intrusion where M is maximised. We define class U as undiluted plume fluid corresponding to the source region $\mathcal{U} = \{M < 0\}$, introduced in the definition of QSS in § 4.5. For convenience, we use the notation $\{M < 0\}$ as shorthand for $\{(b, \phi)|M(b, \phi; t) < 0\}$ henceforth. The mixing flux vectors point along the source line, indicating that mixing within $\mathcal{U}$ is mostly within the plume rather than between the plume and environment, owing to the shielding effect. Once undiluted plume fluid is exposed to the environment, there is a strong mixing flux between $\mathcal{U}$ and the $\phi = \phi_{min}$ axis where environmental fluid joins the distribution.

As discussed in § 4.1, we expect volume to accumulate in some region of buoyancy-tracer space. This is clearly demonstrated in physical space, where fluid collects in the intrusion after mixing with the environment. We can distinguish the accumulation region from the 'transport' region through which volume moves to reach the accumulation region by identifying a region in which M is small and approximately constant. In this region, plume fluid is actively mixing with the environment and transporting volume away from the source line, but fluid does not accumulate in this region. Then, fluid that has undergone significant mixing and accumulates in the intrusion corresponds with a region where M is increasing with time. The regions are distinguished by a time-dependent threshold $m^*(t)$ such that the transport region, where much of the transition from undiluted to mixed plume fluid occurs, is $\mathcal{T} = \{0 < M \leqslant m^*\}$ and we refer to fluid corresponding to this region as class T. The accumulation region is $\mathcal{A} = \{M > m^*\}$ with corresponding mixed fluid accumulating in the intrusion referred to as class A. The threshold $m^*(t)$
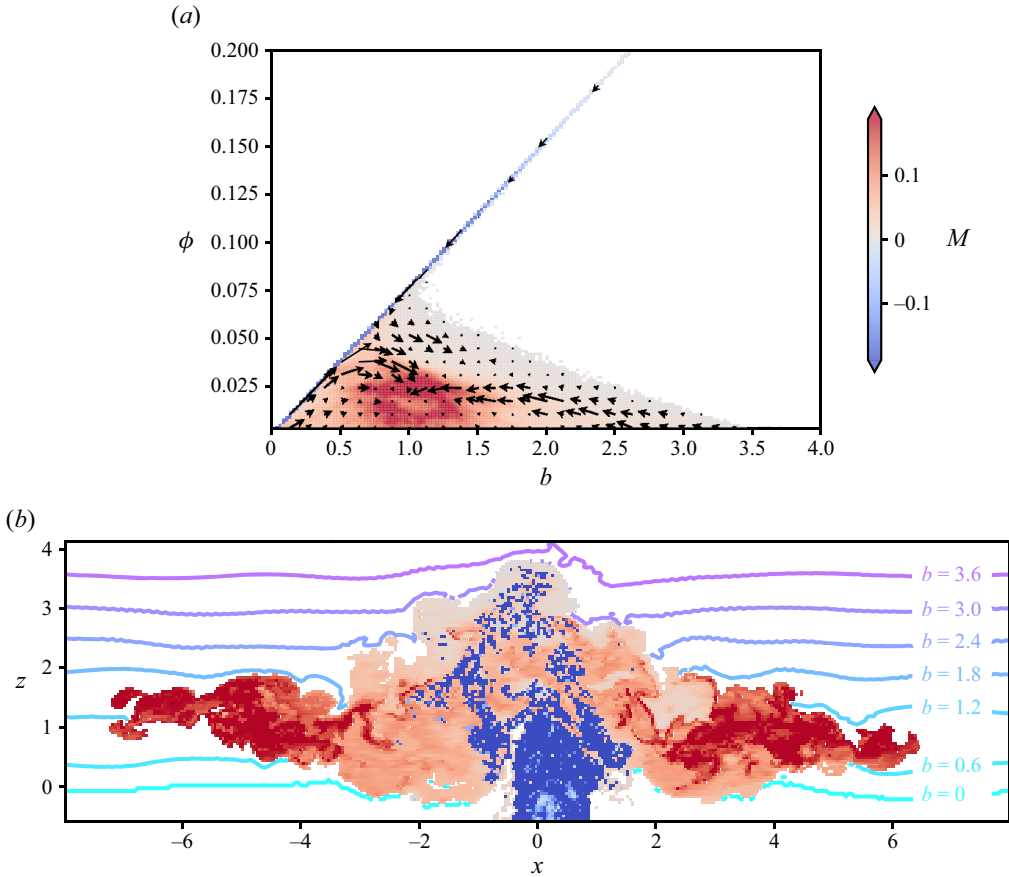
(*a*)

(*b*)

Figure 9. Snapshots at non-dimensional time $t = 14$ of the buoyancy-tracer net mixing effect distribution, $M(b, \phi; t)$, in buoyancy-tracer space (*a*) and (*b*) in an $x - z$ cross-section of physical space. Buoyancy contours are shown in the surrounding environment. The mixing flux distribution, $\boldsymbol{F}$, is overlaid in the top panel and the vectors are uniformly scaled to be visible.

is found by identifying the value m which minimises the total mixing flux convergence $f(m; t)$ associated with a region $\{0 < M \leqslant m(t)\}$ at each time t, where

$$f(m; t) = \int_{\{0 < M \leqslant m\}} \frac{\mathrm{d}W}{\mathrm{d}t} - S \, \mathrm{d}b \, \mathrm{d}\phi = - \int_{\{0 < M \leqslant m\}} \boldsymbol{\nabla}_{(b,\phi)} \cdot \boldsymbol{F} \, \mathrm{d}b \, \mathrm{d}\phi, \qquad (4.13)$$

so that the volume that enters the region $\mathcal{T}$ is approximately equal to the volume leaving $\mathcal{T}$. Then, remaining mixed fluid lies in the region $\mathcal{A}$ which must capture the accumulation of mixed fluid, formed from undiluted plume fluid that has entered the stratified layer and entrained environmental fluid. The numerical implementation of this method using the discrete form of the volume distributions is discussed further in Appendix D. The time variation of the threshold $m^*(t)$ is shown in figure 19 in Appendix D.

The net mixing effect distribution with this partitioning is shown in figure 10, with class U coloured blue, class T coloured green and class A coloured red. Within classes U and A, the volume-weighted centre of mass is shown by a coloured triangle, approximately indicating the position in buoyancy-tracer space towards which mixing acts to move fluid within each class. Internal plume mixing of undiluted plume fluid redistributes volume on

997 A48-18

(a)

(b)
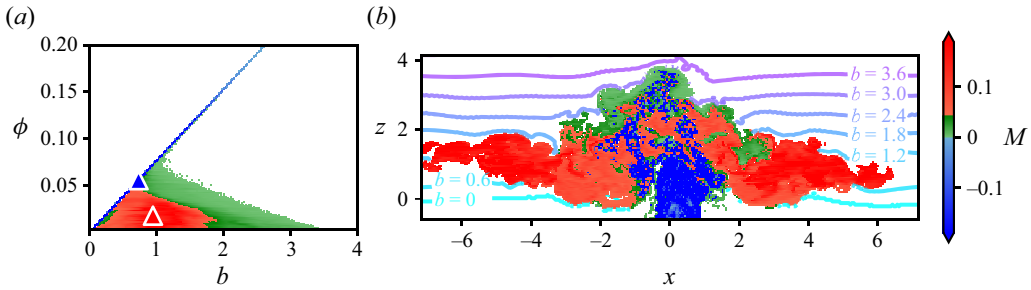
Figure 10. As in figure 9, with the distribution partitioned into three regions: $\mathcal{U}$ (blue) where $M \leqslant 0$, $\mathcal{T}$ (green) where $0 < M \leqslant m^*(t)$ and $\mathcal{A}$ (red) where $M > m^*(t)$. The threshold $m*(t)$ minimises the total mixing flux convergence defined by (4.13). Corresponding fluid classes U, T and A (respectively) shown in physical space. Triangles represent the volume-weighted centre of mass in class U (blue) and class A (red). Undiluted plume fluid in $\mathcal{U}$ is mixed towards the blue triangle whilst fluid accumulating in $\mathcal{A}$ is mixed towards the red triangle.

the source line towards the blue triangle and homogenisation of mixed fluid in the intrusion accumulates volume near the red triangle. Figure 10 demonstrates the correspondence between the regions $\mathcal{U}$, $\mathcal{T}$ and $\mathcal{A}$ and coherent structures of the plume. The source region $\mathcal{U}$ identifies the rising undiluted plume. The accumulation region $\mathcal{A}$ identifies the radially spreading intrusion. The transport region $\mathcal{T}$ corresponds with newly generated mixtures in the plume cap and subsiding fluid joining the intrusion. The partition of the full plume volume into the undiluted plume, plume cap, and intrusion volume is shown in figure 8(b) for $t > t_{QSS}$. As expected, we find that the volume of the intrusion (class A) dominates the plume at late times, as the volume of undiluted plume fluid and the plume cap each remain approximately constant.

4.7. *Entrainment*

We calculate the entrained volume $E(t)$ as the difference between the volume of the full plume and the cumulative volume of the source term S up to time t, so that E represents the volume of environmental fluid that has been mixed into the plume up to time t. We have

$$E(t) \equiv \int_{\{W>0\}} W(b, \phi; t)\, \mathrm{d}b\, \mathrm{d}\phi - \int_0^t \int_{\{W>0\}} S(b, \phi; t')\, \mathrm{d}b\, \mathrm{d}\phi\, \mathrm{d}t' \qquad (4.14)$$

$$= - \int_0^t \int_{\{W>0\}} \nabla_{(b,\phi)} \cdot F(b, \phi; t')\, \mathrm{d}b\, \mathrm{d}\phi\, \mathrm{d}t' \qquad (4.15)$$

$$= \int_0^t \int_{\{\phi=\phi_{min}\}} F_\phi(b, 0; t')\, \mathrm{d}b\, \mathrm{d}t' \approx \sum_{t'} \sum_i \frac{F_{i,j=0}^\phi(t')}{\Delta\phi} \Delta t', \qquad (4.16)$$

where the second equality follows from time integrating (4.2) and the final equality follows from Green's theorem and the fact that the mixing flux F vanishes on the boundary of the $\{W > 0\}$ region except on the surface $\phi = \phi_{min}$ where environmental fluid enters the volume distribution via entrainment. The numerical calculation of E using the discrete form of the mixing flux distribution F_{ij}^ϕ is given by (4.16).

A common definition of an 'entrainment profile' with respect to height is the fractional volume (or mass) increase with height (e.g. de Rooy *et al.* 2013). This is not a useful definition in the case where the plume overturns, since the rate of change with height

captures multiple components of the plume which act to entrain fluid in (potentially) different ways. Exploiting the linear increase of buoyancy with height in the initially linearly stratified environment, we treat buoyancy as a rough proxy for height and define an entrainment profile with respect to buoyancy

$$e(b_i, t) = \int_0^t F_\phi(b_i, 0; t') \, dt' \approx \sum_{t'} \frac{F_{i,j=0}^\phi(t')}{\Delta\phi\Delta b} \Delta t', \qquad (4.17)$$

which represents the volume of environmental fluid entrained up to time t per unit buoyancy. We can then define the volume entrained into a region $\mathcal{R}$ of buoyancy-tracer space which intersects the $\phi = \phi_{min}$ boundary as

$$E(\mathcal{R}, t) = \int_0^t \int_{\{\phi=\phi_{min}\}\cap\mathcal{R}} F_\phi(b, 0; t') \, db \, dt' = \int_{\{\phi=\phi_{min}\}\cap\mathcal{R}} e(b, t) \, db, \qquad (4.18)$$

which is numerically calculated by summing over the indices i in (4.17) which belong to the intersection of $\mathcal{R}$ with the boundary $\phi = \phi_{min}$. We define the entrainment rate as the time rate of change of the entrained volume into a region $\mathcal{R}$, i.e. $\dot{E}(\mathcal{R}) = \partial_t E(\mathcal{R})$. This quantifies the rate at which volume is entrained into a physical volume represented by a region $\mathcal{R}$ in buoyancy-tracer space. Whilst we expect vigorous mixing at the boundary between a sub-volume of the plume and the environment to result in entrainment, the entrainment rate $\dot{E}$ does not necessarily quantify this since larger volumes would be expected to entrain more volume over time even if the 'strength' of the mixing is weaker. To quantify the strength of the entrainment into each sub-volume of physical space corresponding to a partitioning of buoyancy-tracer space, we define the specific entrainment rate as the ratio of the entrainment rate with the volume of each sub-region itself, i.e. $\dot{E}(\mathcal{R})/V(\mathcal{R})$ for each region $\mathcal{R} = \mathcal{U}, \mathcal{T}, \mathcal{A}$.

Figure 11 shows the evolution of the entrainment profile through the simulation. Significant entrainment occurs over a large range of intermediate buoyancy values, indicating that most entrained volume is from the environmental fluid surrounding the intrusion. Using the partitioning introduced in §4.6, the entrained volume can be decomposed into the volume entrained into the plume cap $E(\mathcal{T})$, the volume entrained into the intrusion $E(\mathcal{A})$ and the volume entrained just before penetrating the stratified layer $E(\mathcal{U})$. Figure 12(a) shows the entrained volume as well its decomposition. Here, a correction has been made to $E(t)$ to account for numerical artefacts – see Appendix B for details. Figure 12(b) shows the entrainment rate in each of the regions $\mathcal{U}, \mathcal{A}$ and $\mathcal{T}$. The relative contribution of plume cap entrainment and 'lateral' entrainment in the intrusion to the overall entrainment is noted as an open question in the study of fountains by Hunt & Burridge (2015), where the plume cap is analogous to the 'fountain top'. Here, we find that the contribution to the entrained volume from the plume cap (class T) is weak compared with the intrusion (class A) when in QSS. Under the definition of QSS for this flow given in §4.5, volume continuously accumulates in the intrusion and hence the volume of the intrusion dominates the volume of the full plume at late times. Since the intrusion spreads radially, there is a greater contact area between the intrusion and the surrounding environmental fluid compared with the plume cap and the rising plume. This allows a greater volume of environmental fluid to be entrained into the intrusion. This suggests that entrainment of environmental fluid from the lower part of the stratified layer into the intrusion is important for setting the centre of mass of the QSS buoyancy-tracer distribution. However, mixing during the overturning process in the plume cap near z_{max} is important for setting the maximum accessible buoyancy of the volume distribution after
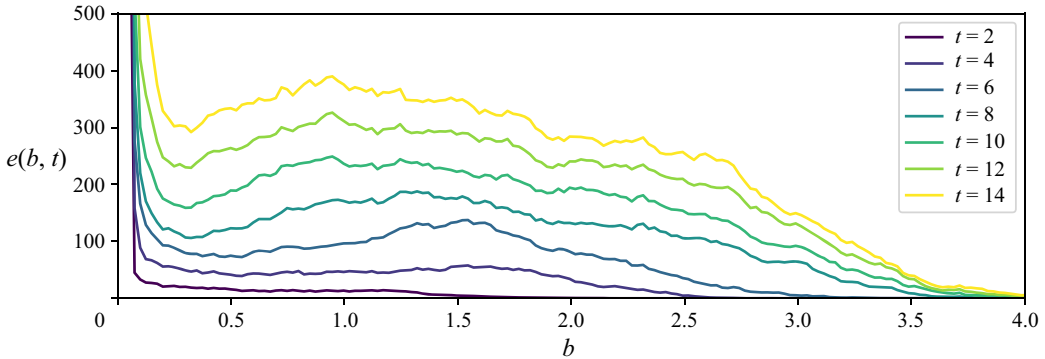
Figure 11. Entrainment profile $e(b, t)$ defined by (4.17) at fixed time intervals post-penetration. The value $e(b, t)$ is the volume of environmental fluid entrained up to time t, per unit buoyancy, as a function of buoyancy b.
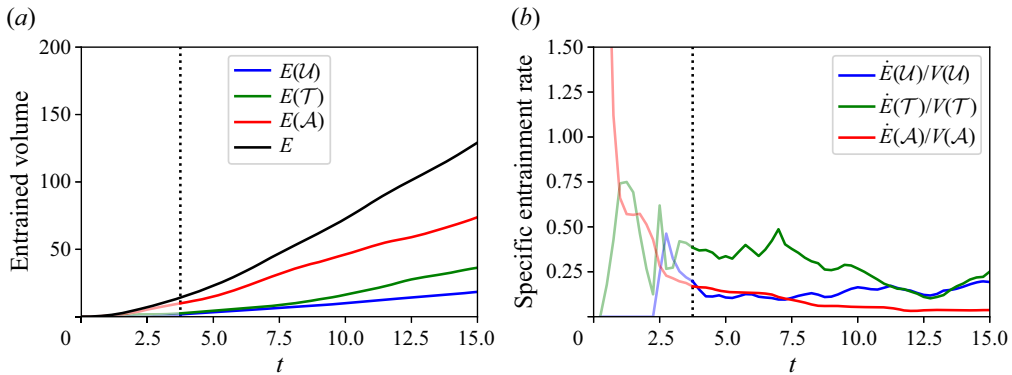

Figure 12. (*a*) Volume of environmental fluid entrained up to time t (black line) and its decomposition into entrainment into the regions $\mathcal{U}$, $\mathcal{T}$ and $\mathcal{A}$ (coloured lines). These regions are defined in § 4.6 and the entrained volumes $E(\mathcal{U})$, $E(\mathcal{T})$ and $E(\mathcal{A})$ are computed using (4.18). (*b*) Specific entrainment rate in each class, defined as the ratio of the rate of change of the entrained volume and the volume, e.g. $\dot{E}(\mathcal{U})/V(\mathcal{U})$. In both plots, the vertical dotted line indicates the start of the QSS.

mixing, and therefore the extent of the accumulation region in buoyancy-tracer space. The specific entrainment rate is larger in class T than in class A, indicating stronger mixing with the environment in the plume cap in QSS compared with the intrusion.

4.8. *Three-stage mixing process*

Together, the results presented in this section suggest a multi-stage mixing process in QSS convective penetration. This is summarised in figure 13, in which we show schematics of the volume distribution partitioned into three regions $\mathcal{U}$, $\mathcal{T}$ and $\mathcal{A}$ of buoyancy-tracer space, and the corresponding classes of fluid in cross-sections of the plume. Fluid moves through each stage of mixing from left to right, corresponding with an increasing value of the net mixing effect M, though occasionally the primary mixing stage may be skipped – see following discussion. In each stage, the convex envelope of fluid involved in mixing is indicated by a grey dashed line in (b, ϕ)-space; arrows in (b, ϕ)-space indicate the movement of individual fluid parcels due to the mixing process; and circular arrows in the $x - z$ cross-section indicate the location of mixing in physical space. These circular arrows are illustrative and are not intended to indicate the physical nature of the mixing

mechanism in each stage. In the secondary mixing stage where multiple mixing processes occur simultaneously, three arrow types are shown which correspond between physical and buoyancy-tracer space. The mixing stages in QSS convective penetration are as follows:

(i) Mixing within the rising plume as undiluted plume fluid penetrates into the stratified layer. This fluid is shielded from the surrounding environment. Thus, in buoyancy-tracer space, internal mixing of undiluted plume fluid acts within $\mathcal{U}$ only, homogenising the distribution and consequently moving fluid towards the centre of mass of class U indicated by the blue triangle in figure 10. This sets the buoyancy-tracer characteristics of plume fluid that is first exposed to environmental fluid near z_{max}.

(ii) Primary mixing between the plume and environment occurs in the plume cap. This mixing may extend below the plume cap into the intrusion as the mixing time scale is slow compared with the dynamical time scale. In buoyancy-tracer space, the primary mixing stage acts on the undiluted plume fluid concentrated near the class U centre of mass and the surrounding environmental fluid with values of buoyancy close to $b = z_{max}$. The resulting mixtures are transported towards intermediate values of buoyancy as indicated by the mixing flux distribution in figure 9(*a*).

(iii) After primary mixing with the environmental fluid, subsiding mixed fluid joins the intrusion and homogenises with its surroundings, moving from class T to class A (dashed arrows). A number of mixing processes act on the fluid accumulating in class A. In buoyancy-tracer space, mixing occurs between four regions of fluid as indicated by the convex envelope in figure 13. Secondary mixing with the environment occurs as environmental fluid lower in the stratified layer is entrained into the intrusion as it spreads (solid arrows), dominating the volume entrained by the full plume at late times. At the edges of the rising plume, undiluted plume fluid mixes with fluid already in the intrusion, resulting in some fluid parcels moving directly from class U to class A without entering the primary mixing stage (dotted arrows) as seen in figure 9(*a*). Finally, mixing in the interior of the intrusion homogenises the buoyancy-tracer distribution of fluid that accumulates within region $\mathcal{A}$. As fluid moves radially, large volumes of fluid in class A are concentrated near the centre of mass in (b, ϕ)-space, where M (and W) are largest.

5. Mixing diagnostics

In this section we use the partitioning introduced in § 4 to examine the statistics of mixing in each stage of the plume evolution.

5.1. *Characterising mixing*

To characterise the physical nature of the mixing in each stage, we consider the mixing efficiency which relates the total energy expended in turbulent mixing with the actual mixing achieved (e.g. Davies Wykes, Hughes & Dalziel 2015). The most useful definition depends on context, e.g. Gregg *et al.* (2018) for oceanographic contexts and Chemel & Staquet (2007) for an atmospheric setting. In buoyancy-driven stratified flows, the mixing efficiency is quantified by utilising the partitioning of potential energy into available potential energy (APE) and background potential energy (BPE). For an incompressible, Boussinesq flow BPE is the potential energy that is not available to do work whilst APE represents the energy stored in the buoyancy field if the flow is not in gravitational equilibrium (Lorenz 1955; Davies Wykes *et al.* 2015). Turbulent mixing irreversibly
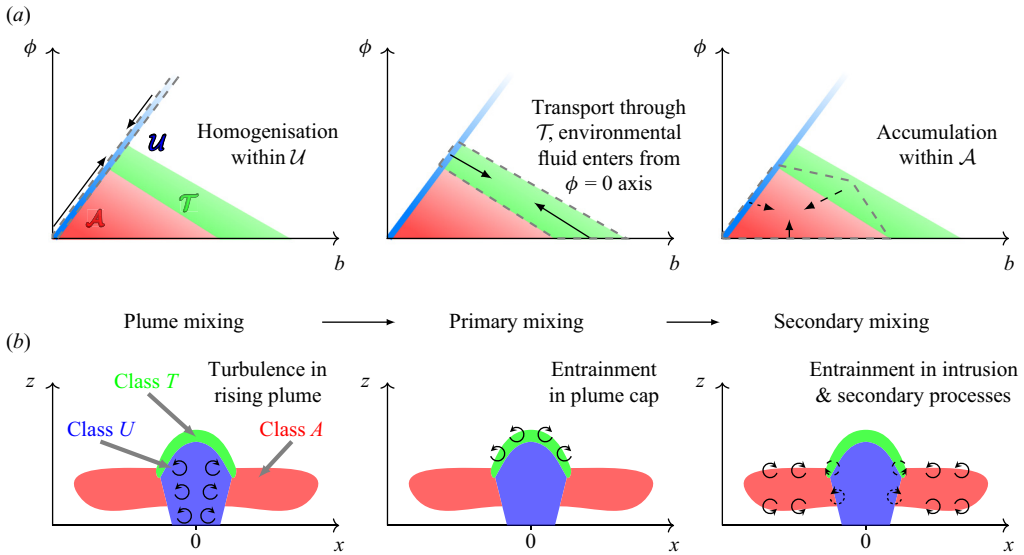
Figure 13. Schematic of the three-stage mixing process in QSS convective penetration of a buoyant plume into a stably stratified layer, identified by the partitioned buoyancy-tracer volume distribution. Buoyancy-tracer space is shown on the top row, with arrows indicating the movement of volume within each mixing stage. The region of buoyancy-tracer space affected by mixing in each stage is indicated by a grey dashed envelope. Physical space is shown on the bottom row with circular arrows indicating where mixing is located. In the secondary mixing stage the three distinct mixing processes are shown as dotted, dashed and solid arrows, both in physical and buoyancy-tracer space.

converts APE into BPE and results in dissipation of turbulent kinetic energy (TKE). The conversion of APE into BPE quantifies the energy expenditure that results in mixing of the buoyancy field and its sum with the TKE dissipation represents the total energy expended by turbulent mixing. The ratio of these two quantities forms the mixing efficiency. Following Howland, Taylor & Caulfield (2020) and Holliday & McIntyre (1981), in the case where $\partial_z b$ is constant in the initial stratified environment we may treat the quadratic form of the potential energy

$$E_p = \tfrac{1}{2}\langle b'^2 \rangle, \tag{5.1}$$

as a proxy for APE. Here, $b'(\boldsymbol{x}, t) = b(\boldsymbol{x}, t) - z$ is the departure from the linear initial stratification and $\langle \cdot \rangle$ denotes a volume average. We refer to E_p as the perturbation potential energy (PE). A full derivation of the perturbation PE budget is given in Appendix E, which follows the derivation as described in Howland *et al.* (2020) except with SGS terms included. The irreversible conversion of perturbation PE to BPE that results from the reduction of buoyancy gradients by mixing is captured by the buoyancy variance dissipation rate

$$\bar{\chi} = \left\langle \kappa_{tot} |\boldsymbol{\nabla} b'|^2 \right\rangle, \tag{5.2}$$

where $\kappa_{tot} = (RePr)^{-1} + \kappa_{SGS}^{(b)}$ is the total diffusivity of buoyancy. The buoyancy variance dissipation rate represents the primary sink of E_p. The total energy dissipated via turbulent mixing is the sum of $\bar{\chi}$ and the dissipation rate of TKE

$$\bar{\varepsilon} = \left\langle \nu_{tot} \frac{\partial u_i}{\partial x_j} \frac{\partial u_i}{\partial x_j} \right\rangle, \tag{5.3}$$

where $v_{tot} = Re^{-1} + v_{SGS}$ is the total viscosity. The TKE dissipation rate acts as the primary sink of TKE. The instantaneous mixing efficiency η is then

$$\eta = \frac{\bar{\chi}}{\bar{\chi} + \bar{\varepsilon}}, \tag{5.4}$$

as in e.g. Howland *et al.* (2020) and Peltier & Caulfield (2003). Here, we use an overbar to denote a volume averaged quantity. It is instructive to examine the spatial structure of the dissipation rates. In particular, regions of large χ indicate intense buoyancy gradients and regions of large ε indicate intense turbulent motion.

Further information on the state of turbulence in stratified flows is often drawn from the buoyancy Reynolds number $Re_b \equiv \langle \varepsilon \rangle / v N^2$. We define a pointwise activity parameter I and its mean $\bar{I}$

$$I = \frac{\overline{\frac{\partial u_i}{\partial x_j} \frac{\partial u_i}{\partial x_j}}}{\left| \frac{\partial b}{\partial z} \right|} = \frac{\varepsilon}{v_{tot} \left| \frac{\partial b}{\partial z} \right|}, \quad \bar{I} = \frac{\langle \varepsilon / v_{tot} \rangle}{\left\langle \left| \frac{\partial b}{\partial z} \right| \right\rangle}. \tag{5.5a,b}$$

The bulk property $\bar{I}$ is analogous to Re_b except with SGS contributions to viscosity included. Also, we replace the global buoyancy time scale N^{-1} with a local measure of the buoyancy time scale $|\partial_z b|^{-1}$ given by the local buoyancy gradient. This is a more appropriate measure since buoyancy gradients within the plume differ significantly from the background linear stratification and are more representative of the regime in which mixing occurs inside the plume. As with Re_b, the mean activity parameter $\bar{I}$ can be interpreted as the ratio of the destabilising effects of turbulent stirring to the stabilising effects of buoyancy and viscosity. Similarly, I may be treated as the ratio of the (local) buoyancy time scale $(\partial b/\partial z)^{-1/2}$ to the time scale of development of turbulent effects $(\varepsilon/v_{tot})^{-1/2}$ (Ivey, Winters & Koseff 2008). Regions of large I indicate active turbulence (García-Villalba & del Álamo 2011) that is weakly affected by stratification.

5.2. *Results and discussion*

Cross-sections in physical space of the dissipation rates ε and χ, activity parameter I and local buoyancy gradient $\partial_z b$ are shown in figure 14. These diagnostics are only shown in the plume, where $\phi > \phi_{min}$. In the surrounding environment, buoyancy contours are shown. The mixing diagnostics within the plume structures identified by classes U, T and A are quantified by histograms separated into each class in figure 15. The colours for each class correspond with those used in § 3 (e.g. figure 13). The black dashed lines show the histograms for the full plume, i.e. all fluid within the stratified layer where $\phi > \phi_{min}$. This full histogram is normalised to form a p.d.f. The partitioned histograms are scaled so that the sum of the class U, T and A histograms equals the full plume p.d.f. These histograms are summarised by volume averages of the mixing diagnostics within each class, as well as the full plume volume average, in table 2.

The histograms for TKE dissipation in figure 15(*a*) and buoyancy variance dissipation in figure 15(*c*) are further separated based on where v_{SGS} and κ_{SGS}, respectively, are non-zero or vanish. This distinction is made since the total viscosity v_{tot} and total dissipation κ_{tot} are bimodal with a peak where the SGS contribution vanishes (where the simulation effectively switches from LES to direct numerical simulation, such that v_{tot} and κ_{tot} reduce to the molecular values) and a peak where the SGS contribution is non-zero – see figures 15(*b*) and 15(*d*). The separation of the histograms based on non-zero and zero
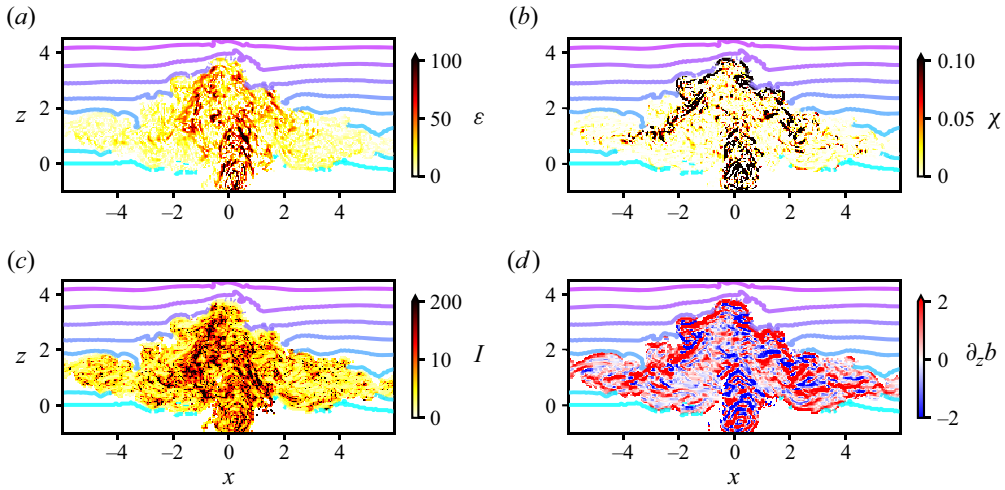
Figure 14. The $x - z$ cross-sections of the mixing diagnostics ε, χ, I and $\partial_z b$ within the plume, where $\phi > \phi_{min}$ at non-dimensional time $t = 14$. Mixing diagnostics are defined in §5.1. Cross-sections are taken at the plume centreline. Buoyancy contours are shown outside the plume.

	Full plume	Class U	Class T	Class A
Volume %	100	3.64	9.88	8.65
Activity parameter $\bar{I}$	16.8	81.6	18.8	12.8
Vertical buoyancy gradient $\langle |\partial_z b| \rangle$	1.29	1.41	2.88	1.11
TKE dissipation rate $\bar{\varepsilon}$	0.0466	0.347	0.127	0.0247
Buoyancy variance dissipation rate $\bar{\chi}$	0.0238	0.0595	0.129	0.0103
Instantaneous mixing efficiency η	0.339	0.147	0.504	0.294

Table 2. Volume-averaged mixing quantities $\varepsilon, \chi, I, \partial_z b$ and mixing efficiency η defined in §5.1 at $t = 15$. Averages are computed over the full plume and within class U, T and A. The percentage of the full plume volume associated with each class is given to indicate the relative contribution of each class to the full plume average.

SGS contribution demonstrates that the bimodality of the histograms for ε and χ is a consequence of the bimodal total viscosity and diffusivity alone. The vertical buoyancy gradient histogram is shown on a logarithmic scale since the most extreme values are rare but remain important for mixing.

The results show that the mixing statistics are quantitatively different in each class, suggesting that the mixing regimes differ in each of the three stages of the plume evolution highlighted in §4.8. The cross-sections in figure 14 show that TKE dissipation ε is particularly large in the rising undiluted plume and in some regions of the plume cap. This is supported by the histograms which show that TKE dissipation is an order of magnitude larger in class U and T compared with class A. The activity parameter is also largest in the rising undiluted plume but comparable in the plume cap and intrusion. The largest values (both positive and negative) of the vertical buoyancy gradient $\partial_z b$ are found in the plume cap (class T) with a clear positive bias. The relatively tighter spread of the $\partial_z b$ distribution in class U in figure 15(f) suggests that smaller vertical buoyancy gradients are more common in the undiluted plume fluid as compared with the plume cap and intrusion. This explains the increased magnitude of the activity parameter in class U compared with
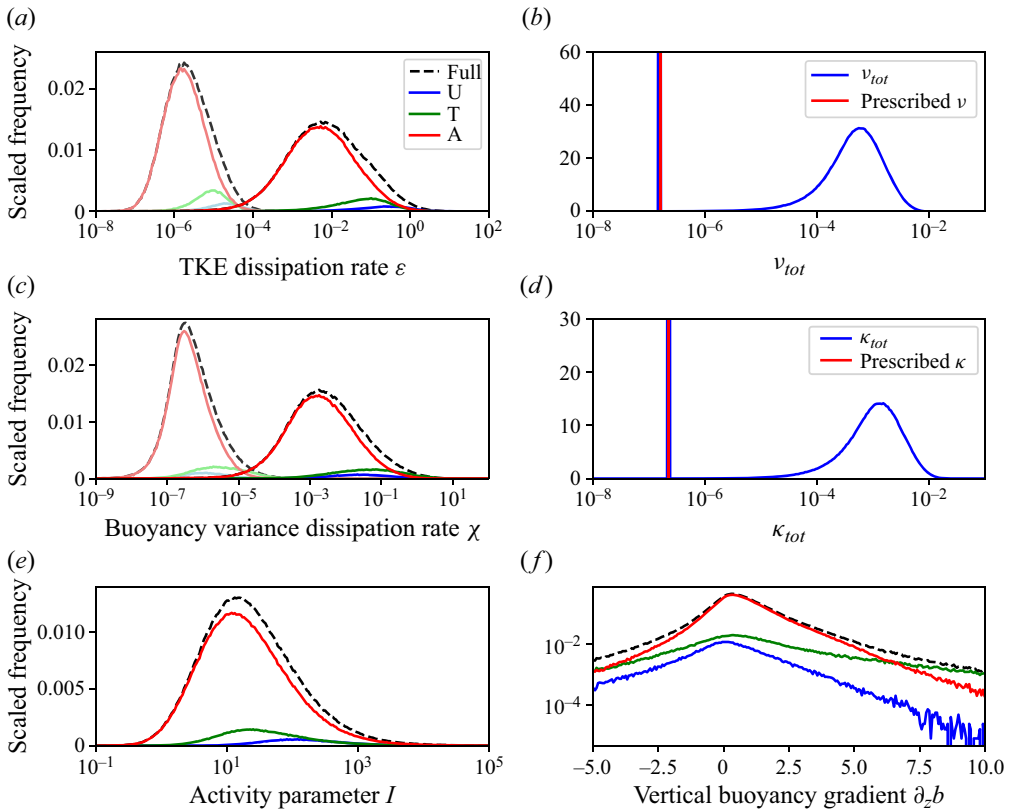
Figure 15. (a,c,e,f) Histograms of the mixing diagnostics ε, χ, I and $\partial_z b$ defined in § 5.1 (black dashed line) decomposed into histograms within class U, T, A (coloured lines). The histograms within each class are scaled so that their sum is the histogram of the full plume. In (a,c), the histograms are further separated into those with $\nu_{SGS} = 0$ and $\kappa_{SGS}^{(b)} = 0$ (light colours) and with ν_{SGS} and κ_{SGS} non-zero (usual colours). (b,d) Histograms of the total viscosity ν_{tot} and total buoyancy diffusivity κ_{tot} respectively. All histograms are computed at $t = 15$. All vertical axes show the scaled histogram frequency. The scaling is such that the total area is unity for the full plume histograms and the sum of the partitioned histograms equals the full plume histogram. Similarly in (b,d) the frequency is scaled so that the total area is unity.

class T despite similar magnitudes of TKE dissipation; ε is large in both classes but $\partial_z b$ is generally larger in class T and hence I, proportional to the ratio $\varepsilon/\partial_z b$, is smaller in class T. The strongest buoyancy gradients as measured by χ are found in the primary mixing region (class T), where fluid overturns and subsides fluid in the plume cap. Intense buoyancy gradients are also found in the rising column of undiluted plume fluid, but χ is more sparse here than in the plume cap. The strong buoyancy gradients found at the top edge of the plume cap are a result of the relatively less buoyant plume impinging on the more buoyant surrounding environmental fluid. Note that the largest values of χ at the extreme positive tail of the full plume p.d.f. are almost all from class T.

We summarise the mixing regimes described by the mixing diagnostics as follows. In class U, we find active turbulence with large dissipation of TKE, consistent with the undiluted plume being unaffected by the surrounding stratified environment due to the shielding effect. Since the undiluted plume fluid becomes well mixed during its rise through the uniform layer, there are relatively small buoyancy gradients. As a result, there is relatively little PE dissipation. In class T, rising plume fluid impinges upon the

997 A48-26

more buoyant surrounding environmental fluid, generating particularly strong vertical buoyancy gradients. Horizontal buoyancy gradients are also generated by overturning. Turbulence advected upwards in class U is carried over into class T but gradually suppressed by the intense buoyancy gradients present in the plume cap, thus reducing the activity parameter. As the turbulent motion stirs these buoyancy gradients, significant PE dissipation occurs and consequently a large mixing efficiency is achieved, around 50 %. Finally in class A, which eventually dominates the volume of the full plume as the intrusion grows, the interior of the intrusion becomes well mixed resulting in weak buoyancy gradients. There is some indication of a weak stratification and layering forming within the intrusion. Secondary mixing processes between the intrusion and environmental fluid at the bottom of the stratified layer can introduce larger vertical buoyancy gradients and result in some PE dissipation. Overall, TKE dissipation is weak as the buoyant forces driving turbulent motion are weakened by earlier mixing. Whilst both TKE and PE dissipation are weak in class A, they are of similar magnitude and hence a greater mixing efficiency is achieved compared with class U. This could be attributed to the continued entrainment of environmental fluid above and below the intrusion, introducing small-scale buoyancy gradients which are acted upon by the weak turbulent motion.

6. Conclusions

In this paper we have analysed a LES of a buoyant pure plume penetrating into a linearly stably stratified layer. We have outlined the buoyancy-tracer volume distribution formalism to examine tracer transport via turbulent mixing. Using this formalism, we developed a method for objectively partitioning buoyancy-tracer space into three regions based on the net change in volume due to mixing. Each of these regions identifies corresponds with a class of fluid lying in coherent regions of the plume in physical space. The method distinguishes undiluted plume fluid (class U) from mixtures of plume and environmental fluid. Mixed fluid is further partitioned into newly generated mixtures in the plume cap that are actively mixing with the environment (class T), and fluid in the radially spreading intrusion that has already undergone significant mixing (class A). In buoyancy-tracer space, the intrusion corresponds with an accumulation region (corresponding with class A) where volume collects and homogenises. Active mixing with the environment in the plume cap moves volume from the source region, through a transport region (corresponding with class T), into the accumulation region. The accumulation region represents the majority of the plume volume at late times. To quantify the mixing regime in each class of fluid, we use the buoyancy variance dissipation rate, TKE dissipation rate, vertical buoyancy gradient and an activity parameter as diagnostic variables in each sub-volume of the plume. The instantaneous mixing efficiency is also calculated by treating the buoyancy variance dissipation rate as a proxy for the energy dissipated in turbulent mixing that actually results in mixing of buoyancy.

Our results demonstrate a three-stage mixing process in QSS penetration of a plume into a stably stratified layer. In the first 'plume mixing' stage (class U), turbulence within the undiluted rising plume homogenises the buoyancy-tracer distribution as fluid rises into the stratified layer. The turbulent motion near the centreline of the plume is relatively unaffected by the surrounding stratification owing to a shielding effect from the plume edge and surrounding intrusion. This homogenisation process sets the range of buoyancy and tracer concentration which is first exposed to the environment when fluid overturns near the maximum penetration height. The 'primary mixing' stage occurs as rising fluid impinges on the more buoyant environment, establishing intense

buoyancy gradients in the plume cap (class *T*). The mixing of undiluted plume fluid with the surrounding environment near z_{max} has a particularly large mixing efficiency. The maximum penetration height approximately determines the buoyancy of the environmental fluid involved in the primary mixing stage and sets the extent of the buoyancy-tracer convex envelope for the remainder of the mixing process. As newly generated mixed fluid joins the intrusion and homogenises with fluid already in the intrusion (class *A*), the intensity of turbulence decreases and buoyancy gradients weaken. Several secondary mixing processes occur in the intrusion. This includes the entrainment of environmental fluid surrounding the intrusion, and mixing with small amounts of undiluted plume fluid at the edge of the rising plume that immediately join the intrusion without entering the plume cap. The volume of environmental fluid entrained into the intrusion during QSS dominates the volume into the plume as a whole at late times, but entrainment in the plume cap is 'strongest' in the sense of the largest fractional rate of increase in volume.

The statistical properties of turbulence are different in each of the three stages. The undiluted plume core is the most turbulent (as measured by the activity parameter) with TKE dissipation significantly larger than PE dissipation. In the plume cap, the intense buoyancy gradients result in large PE dissipation and small TKE dissipation and hence the entrainment of the surrounding environment achieves a large mixing efficiency, with around 50 % of the total energy dissipated by turbulence resulting in mixing. As mixed fluid homogenises in the intrusion and further environmental fluid is entrained, weak buoyancy gradients are continually introduced and eroded by weak turbulence with low TKE dissipation. The mixing efficiency in the intrusion is moderately large, though smaller than in the plume cap.

Models of convective penetration which cannot resolve the processes responsible for mixing and entrainment must parameterise the effects of mixing on the flow. The markedly different statistics in each class suggest that each stage of mixing should be parameterised separately. Parameterisations of mixing in convective penetration could exploit the changing proportion of the full plume volume in each sub-region. For example, at early times before the formation of an intrusion, the plume is dominated by undiluted plume fluid in the plume core with intense turbulence but the mixing efficiency is small. At late times as fluid accumulates in the intrusion, the plume volume is dominated by the intrusion with weaker buoyancy gradients and turbulence and a greater mixing efficiency. Therefore the turbulent statistics associated with the full plume volume must change over time.

The partitioning method presented here, as well as the buoyancy-tracer volume distribution formalism as a whole, offers a way to analyse mixing in numerical simulations of stratified flows. Physical arguments can be made that restrict the regions of buoyancy-tracer space accessible via mixing and consideration of terms in the volume distribution budget equation (4.2) highlight the mixing processes that occur and the resulting tracer transport.

Declaration of interests. The authors report no conflict of interest.

Data availability statement. Simulation data and scripts used to generate figures are available upon request.

Author ORCIDs.

- Charles W. Powell https://orcid.org/0000-0001-8129-196X;
- Peter H. Haynes https://orcid.org/0000-0002-7726-6988;
- John R. Taylor https://orcid.org/0000-0002-1292-3756.

Appendix A. Plume generation method

In §2 we introduce the numerical set-up for investigating convective penetration of a buoyant plume into a stably stratified layer. The buoyant plume is generated in a small forcing region at the bottom of the domain with the plume centreline at the middle of the computational domain, $x = y = 0$. We use a volumetric forcing method in which the vertical velocity, buoyancy and tracer concentration are relaxed towards prescribed profiles in the shallow forcing region indicated in figure 1. The prescribed profiles are chosen to be the far-field solutions of the Morton *et al.* (1956) (henceforth MTT) axisymmetric plume equations for a pure plume with source radius r_0 and integral source buoyancy flux $F_0 = 2 \int_0^\infty \bar{w}\bar{b}|_{z=-H} r \, dr$. The plume carries a passive tracer with a source tracer flux that has a dimensional value identical to the source buoyancy flux, i.e. in non-dimensional terms $F_0^{(\phi)} = 2 \int_0^\infty \bar{w}\bar{\phi}|_{z=-H} r \, dr = \mathcal{B}F_0$ where $\mathcal{B} = LT^{-2}$ and this excludes the normalisation of ϕ by its source value on the plume centreline which is performed in post-processing. The term 'pure' plume refers to the relationship between the source fluxes and is quantified in terms of the flux-balance parameter Γ introduced by Morton (1959) and defined as

$$\Gamma = \frac{5 F_b Q^2}{8 \alpha M^{5/2}}, \tag{A1}$$

where α is the entrainment coefficient and the integral volume flux Q, specific momentum flux M and buoyancy flux F_b are defined as

$$Q = 2 \int_0^\infty \bar{w} \, r \, dr, \quad M = 2 \int_0^\infty \bar{w}^2 \, r \, dr, \quad F_b = 2 \int_0^\infty \bar{w}\bar{b} \, r \, dr, \tag{A2a-c}$$

where $\bar{\cdot}$ denotes an azimuthal and time average. Note that in Appendices A and B only we use M, F_b (and F_ϕ in Appendix B) to refer to these integral fluxes, consistent with the notation used in the literature (e.g. Hunt & Kaye 2005; van Reeuwijk *et al.* 2016). A forced plume, in which there is an excess of momentum relative to the buoyancy forcing, has $0 < \Gamma < 1$ and the special case of a pure plume in which the momentum and buoyancy fluxes are balanced has $\Gamma = 1$. The pure plume state is stable to perturbations in the amount of buoyancy supplied (Hunt & Kaye 2005). The vertical profiles $r_m(z)$, $w_m(z)$, $b_m(z)$, $\phi_m(z)$ for the radius, vertical velocity, buoyancy and tracer concentration in the set-up we consider are

$$r_m(z) = \tfrac{6}{5}\alpha(z + H - z_v), \tag{A3}$$

$$w_m(z) = \frac{5}{6\alpha} \left(\frac{9}{10} \alpha F_0 \right)^{1/3} (z + H - z_v)^{-1/3}, \tag{A4}$$

$$b_m(z) = \frac{5 F_0}{6\alpha} \left(\frac{9}{10} \alpha F_0 \right)^{-1/3} (z + H - z_v)^{-5/3}, \tag{A5}$$

$$\phi_m(z) = \frac{5 F_0^{(\phi)}}{6\alpha} \left(\frac{9}{10} \alpha F_0^{(\phi)} \right)^{-1/3} (z + H - z_v)^{-5/3}, \tag{A6}$$

where $z_v = -(5/6\alpha)r_0$ is the virtual origin (which ensures a source radius r_0) and $\alpha = 0.11$ is the entrainment coefficient. Since the source tracer flux is the same as the source buoyancy flux, and b and ϕ evolve identically in the uniform layer up to a linear factor, the profile $\phi_m(z)$ used for the passive tracer is the same as the profile $b_m(z)$ used for the buoyancy except with F_0 replaced by $F_0^{(\phi)}$.

The full structure towards which the vertical velocity, buoyancy and tracer concentration are forced uses the vertical profiles (A3)–(A6) with Gaussian radial profiles of width $r_m(z)$. Gaussian profiles have been shown to approximate experimental data well (List 1982; Papanicolaou & List 1988; Shabbir & George 1994). Tests were carried out with various other radial profiles at the source, all of which result in a Gaussian profile in w, b and ϕ far from the source (but below the stratified layer) where the plume is fully developed. The forcing on w, b and ϕ is then

$$f_w(\boldsymbol{x}, t) = \frac{1}{\tau} \left[w(\boldsymbol{x}, t) - 2w_m(z) \exp\left[-2\frac{x^2 + y^2}{r_m(z)^2} \right] \left(1 + \frac{1}{10}\xi(t) \right) \right] f_m(z), \qquad (A7)$$

$$f_b(\boldsymbol{x}, t) = \frac{1}{\tau} \left[b(\boldsymbol{x}, t) - 2b_m(z) \exp\left[-2\frac{x^2 + y^2}{r_m(z)^2} \right] \left(1 + \frac{1}{10}\xi(t) \right) \right] f_m(z), \qquad (A8)$$

$$f_\phi(\boldsymbol{x}, t) = \frac{1}{\tau} \left[\phi(\boldsymbol{x}, t) - 2\phi_m(z) \exp\left[-2\frac{x^2 + y^2}{r_m(z)^2} \right] \left(1 + \frac{1}{10}\xi(t) \right) \right] f_m(z), \qquad (A9)$$

where $\xi(t)$ is a random number between -1 and 1, used to apply uncorrelated 10 % perturbations to the prescribed profiles at each step (note that the same perturbation is not used for all profiles), to initiate turbulence. The factor $1/\tau$ controls the coupling strength with the momentum equations. The size of τ is arbitrary other than being small enough to control against dynamical variation and large enough to avoid numerical instability. The function $f_m(z)$ constrains the forcing to a thin layer at the base of the domain. We use

$$f_m(z) = \frac{1}{2}\left(1 - \tanh\left(\frac{z + H - L_c}{L_p} \right) \right), \qquad (A10)$$

where L_c is the depth of the forcing region above $z = -H$ and L_p controls how sharply the forcing decays above $z = -H + L_c$. As illustrated in figure 1, $f_m(z) \approx 1$ for $z \lesssim -H + L_c$ and $f_m(z) \approx 0$ for $z \gtrsim -H + L_c$. Whilst the forcing is applied across the entire domain, $f_m(z)$ limits the depth in which the forcing is non-zero and the exponential factor in (A7), (A8) and (A9) constrains the forcing to small radii $x^2 + y^2 \lesssim r_m(z)^2$. An additional perturbation is applied to each velocity component in the two grid layers above $z = -H + L_c$ to initiate turbulence, which develops as the plume rises through the uniform layer. We ensure that the plume has reached self-similarity (i.e. the turbulence and plume structure are fully developed) before penetrating the stratified layer – see figure 18 in Appendix B.

The forcing method detailed here is non-standard. We found the typical method of generating a buoyant plume with a simple buoyancy gradient on the bottom boundary (e.g. Pham *et al.* 2007; van Reeuwijk *et al.* 2016) to be unsuitable owing to pinching of the plume radius close to the bottom boundary where inflow dominates the diffusive boundary buoyancy flux. Pinching reduces control of the source radius and results in excessive numerical artefacts due to the horizontal pseudo-spectral method. Validation of the forcing method detailed here and the numerical scheme detailed in § 2 is discussed in Appendix B.
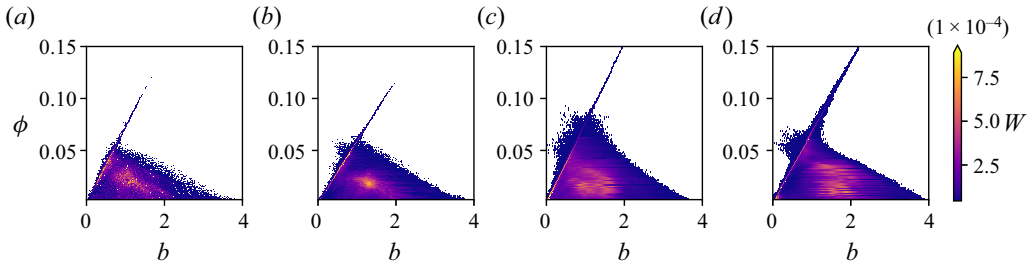
Figure 16. Buoyancy-tracer volume distribution $W(b, \phi; t)$, detailed in § 4, at $t = 10$ in three simulations with resolution $128^2 \times 129$, $256^2 \times 257$, $512^2 \times 513$ and $1024^2 \times 1025$ left to right.

Appendix B. Validating the numerical method

B.1. *Resolution sensitivity test*

We study the problem presented here using LESs. Given the sub-grid scales are parameterised in LES, it is necessary to validate the model to ensure that the quantities of interest are sufficiently well resolved and that the results are not strongly dependent on the model resolution. Here, our primary focus is on the volume distribution in buoyancy/tracer space. Figure 16 shows the volume distribution $W(b, \phi; t)$ at non-dimensional time $t = 10$ for the simulations discussed in § 2 at three resolutions, $128^2 \times 129$, $256^2 \times 257$, $512^2 \times 513$, and $1024^2 \times 1025$, with all other aspects of the simulation set-up fixed. To aid comparison, W is normalised by the full plume volume $\sum_{ij} W_{ij}(t)$ (see § 4.1). The structure of the distribution is similar at all resolutions. There is some noise in the distribution at lower resolution, since the smaller number of grid cells offers a smaller sample of the values of buoyancy and tracer concentration. The only element of the volume distribution structure that notably changes with resolution is the extent of the source line where $b \propto \phi$. This can be attributed to poor representation of the forcing profile at lower resolution; in the forcing region (see figure 1) the plume is thin compared with the width of the domain. This means relatively few grid points cover the plume at lower resolution and hence the forcing profile is poorly captured, in particular the maximum values of b, w and ϕ on the plume centreline are reduced. Therefore, the forcing profile that is achieved often has a smaller associated buoyancy and tracer source flux than the value F_0 prescribed for the simulation and hence the extent of the source line in buoyancy-tracer space is reduced. This is easily accounted for by increasing the prescribed value or decreasing the forcing relaxation time scale τ (see Appendix A). In § 3 we report the value of F_0 computed from the simulation which suitably represents the plume forcing profiles achieved (see Appendix A for a detailed discussion of the forcing method).

B.2. *Numerical artefacts*

In the horizontal pseudo-spectral numerical scheme used by DIABLO, the spectral cutoff filter introduces unphysical oscillations in the scalar fields throughout a horizontal level in response to sharp gradients on the same horizontal level. This is known as Gibbs ringing (e.g. DeBonis 2019) and is qualitatively similar to the oscillations that arise in the Fourier series representation of a finite step function using a finite number of modes. In the simulation we present, these oscillations are relevant in two locations where particularly strong gradients of b and ϕ arise. Firstly, at the top of the uniform layer before the plume penetrates the stratified layer. Here, b and ϕ remain large on the plume centreline (and confined to small radii) whilst they vanish in the surrounding environment, resulting in
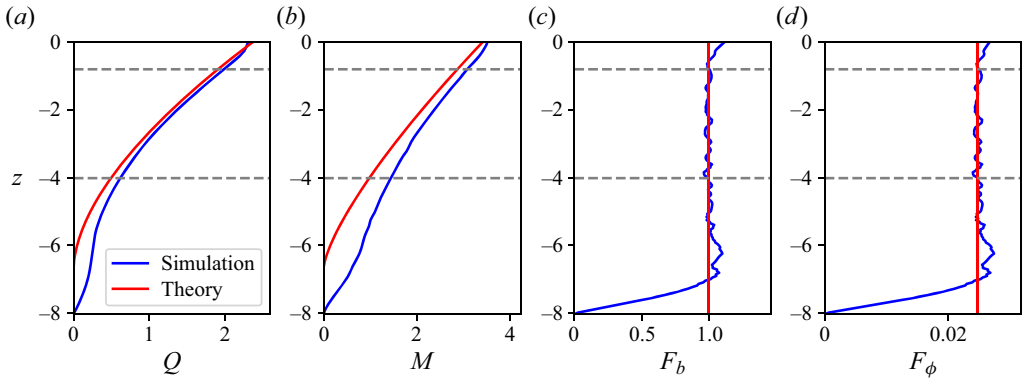
997 A48-31

Figure 17. Integral volume flux Q, specific momentum flux M, buoyancy flux F_b and tracer flux F_ϕ defined in (A2a–c) and (B2) shown in the uniform layer $z \leqslant 0$. Simulation data shown in blue and theoretical predictions for a pure plume (using vertical profiles given in (A3)–(A5) with a Gaussian radial profile) shown in red. Range of heights for which radial profiles are shown in figure 18 indicated by grey dashed lines.

steep gradients in both scalar fields. Note this ringing is present throughout the uniform layer and can be observed in figure 2 at the bottom of the domain in particular, but does not have a significant impact on the plume on average (see azimuthally averaged profiles in figure 18) nor on the simulated buoyancy and tracer fluxes (see figure 17). Secondly, above the intrusion the plume width is small compared with the size of the domain and the plume buoyancy is significantly smaller than the surrounding environment, creating steep gradients in the buoyancy field in particular. The resulting oscillations imprint on the value of the buoyancy in the plume, shifting a small amount of volume away from the source line in buoyancy-tracer space and producing a 'bulge' in the volume distribution W. This is evident in figure 16, particularly panels (c,d). Whilst the effect appears prominent (owing to the colour map), this bulge contains only $0.77\,\%$ of the full plume volume at $t = 10$ in the $512^2 \times 513$ simulation presented in the main paper. The numerical scheme conserves total tracer concentration in the absence of sources and sinks, though difficulties arise in calculating the plume volume that enters the stratified layer, since grid cells with $\phi < \phi_{min}$ are excluded from the calculation of the source distribution S but if the oscillation reverses sign then this tracer may be considered part of the plume. Similarly, the entrained volume $E(t)$ discussed in § 4.7 is underestimated due to these grid cells being excluded from the calculation of F_ϕ. To account for Gibbs ringing, we therefore use the absolute value of the buoyancy and tracer concentration fields, $|b|$ and $|\phi|$, to calculate the source distribution S and the mixing flux distribution F. To aid clarity, we do not show the 'bulge' in the volume distribution W or the net mixing effect distribution M in figures 6, 9 and 10, but include the volume as part of class U when computing the volume of undiluted plume fluid $V(\mathcal{U})$. The regions in physical space corresponding to the erroneous volume are coloured according to the corresponding value of b lying on the source line with the same value of ϕ, i.e. we treat these values of b and ϕ as part of class U and colour them accordingly when showing M in physical space (see figure 9).

B.3. *Plume representation*

We further validate our numerical method by comparing the simulated plume with the canonical plume theory of Morton *et al.* (1956) and direct numerical simulations of plumes in the literature, which themselves have been extensively compared with experimental

studies. The integral plume theory of MTT predicts that in a buoyant plume rising from a point source (or equivalently a source with radius r_0 with a virtual origin at $-z_v$), the radius, vertical velocity, buoyancy and tracer concentration become self-similar with respect to characteristic scales

$$r_m = \frac{Q}{M^{1/2}}, \quad w_m = \frac{M}{Q}, \quad b_m = \frac{F_b}{Q}, \quad \phi_m = \frac{F_\phi}{Q}, \qquad \text{(B1}a\text{–}d\text{)}$$

where the integral volume flux Q, specific momentum flux M and buoyancy flux F_b are defined in (A2a–c) and the tracer flux F_ϕ is defined as

$$F_\phi = 2 \int_0^\infty \bar{w}\bar{\phi}\, r \, \mathrm{d}r, \qquad \text{(B2)}$$

where $\bar{\cdot}$ denotes an azimuthal and time average. Note that in Appendices A and B only we use M, F_b and F_ϕ to refer to these integral fluxes, consistent with the notation used in the literature (e.g. Hunt & Kaye 2005; van Reeuwijk *et al.* 2016). The MTT plume equations may be solved to find the vertical profiles of the characteristic scales in (B1a–d) for a pure plume as given in (A3)–(A5) and from these, vertical profiles for the integral fluxes can be computed. These theoretical predictions are compared with the simulation results in figure 17 which demonstrates good agreement once turbulence in the plume becomes fully developed during rise through the uniform layer.

In figure 18(a) we show vertical profiles of the time and azimuthally averaged vertical velocity $\bar{w}$, buoyancy $\bar{b}$ and tracer concentration $\bar{\phi}$, each normalised by the relevant characteristic scale. The profiles are from the region just below the stratified layer, indicated by the grey dashed lines in figure 17. The evident self-similarity of the plume, and the good convergence towards the experimentally observed radial Gaussian profile shown in black, demonstrate that the turbulent behaviour of the plume is well represented. This is further supported by the self-similarity of the radial momentum, buoyancy and tracer fluxes $\overline{u'w'}$, $\overline{u'b'}$, and $\overline{u'\phi'}$ when normalised by the relevant scales in figure 18(b). Here, u refers to the radial velocity and the prime notation refers to the turbulent component. The integral theory of MTT does not make predictions for these radial fluxes but they are in close agreement with the direct numerical simulations presented in van Reeuwijk *et al.* (2016). Figure 18(c) shows the mean radial velocity $\bar{u}$ which is also in agreement with their direct numerical simulation but with increased spread in the profiles owing to the periodic boundaries in our set-up, which modifies the flow into the plume when compared with open boundaries typically used in numerical simulations of plumes, e.g. van Reeuwijk *et al.* (2016). Nonetheless we show that the entrainment is well captured by considering the mean radial specific volume flux $r\bar{u}$ in figure 18(d). The MTT entrainment hypothesis states $[ru]_{r=\infty} = -\alpha r_m w_m$, where α is the entrainment coefficient, which relates the vertical velocity with the radial inflow. The value of α computed in our numerical simulations is shown in figure 18(d) which demonstrates the entrainment behaviour found in experimental observations of plumes. The turbulent statistics in the plume are further validated by following the analysis presented in van Reeuwijk *et al.* (2016). For example, the precise characteristics of the turbulence are tested by calculating the invariants of the anisotropy tensor as detailed in Lumley & Newman (1977). Our results indicate turbulence with weak anisotropy and axisymmetry (not shown), agreeing with the direct numerical simulations of van Reeuwijk *et al.* (2016).
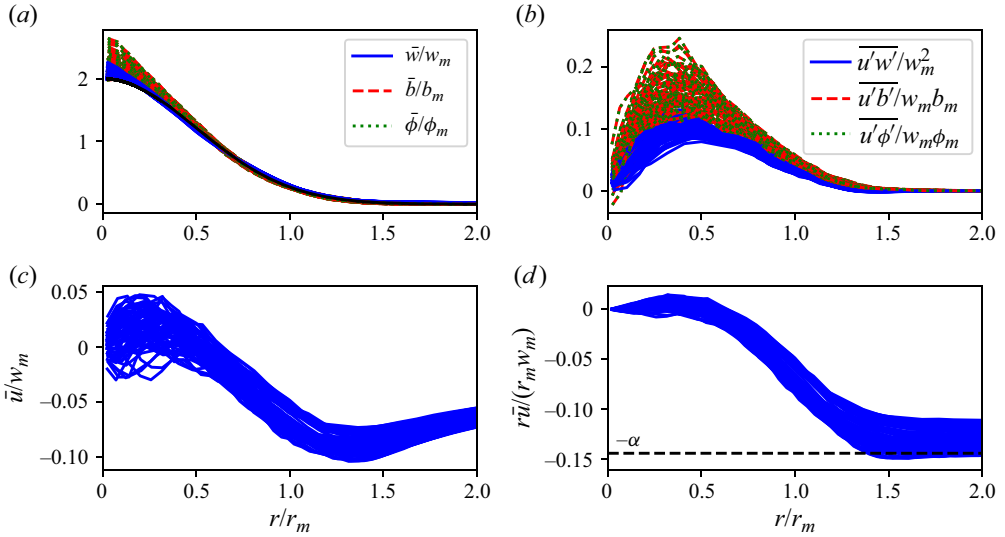
Figure 18. (*a*) Radial profiles of $\bar{w}$, $\bar{b}$ and $\bar{\phi}$. (*b*) Radial profiles of radial momentum flux $\overline{u'w'}$, buoyancy flux $\overline{u'b'}$ and tracer flux $\overline{u'\phi'}$. (*c*) Mean radial velocity $\bar{u}$. (*d*) Mean radial specific volume flux $r\bar{u}$. All data shown in the interval $-5 < z < -1$ in the uniform layer, indicated by grey dashed lines in figure 17. All profiles are self-similar with respect to the relevant scales defined in (B1*a–d*). In panel (*d*), the dashed line indicates the value of the entrainment coefficient α calculated from a linear fit of the plume radius scale r_m and z.

Appendix C. Buoyancy-tracer volume distribution evolution equation

In § 4.1 we define the volume distribution $W(B, \Phi; t)$ and its governing equation

$$\frac{\partial W}{\partial t} = -\nabla_{(B,\Phi)} \cdot \boldsymbol{F} + S, \tag{C1}$$

where $\boldsymbol{F}$ and S represent the flux and boundary source/sink of W, respectively. We derive this evolution equation for the volume distribution W by starting with two scalar fields $b(\boldsymbol{x}, t)$ and $\phi(\boldsymbol{x}, t)$ satisfying

$$\frac{\partial b}{\partial t} + \boldsymbol{u} \cdot \nabla b = \dot{b}, \tag{C2}$$

$$\frac{\partial \phi}{\partial t} + \boldsymbol{u} \cdot \nabla \phi = \dot{\phi}, \tag{C3}$$

with $\nabla \cdot \boldsymbol{u} = 0$. Here, we use $\dot{b}$ and $\dot{\phi}$ to represent general forcing terms which are replaced in § 4.1 with the non-advective forcing on buoyancy b and tracer concentration ϕ. Consider a fixed volume V in which (C2) and (C3) hold and define

$$g_{\mathcal{F}} = \int_V \mathcal{F}(b, \phi) \, \mathrm{d}V, \tag{C4}$$

where $\mathcal{F}(b, \phi)$ is an arbitrary function of b and ϕ. Then

$$
\begin{aligned}
\frac{\partial g_{\mathcal{F}}}{\partial t} &= \int_V \frac{\partial \mathcal{F}}{\partial b} \frac{\partial b}{\partial t} + \frac{\partial \mathcal{F}}{\partial \phi} \frac{\partial \phi}{\partial t} \, \mathrm{d}V \\
&= \int_V \frac{\partial \mathcal{F}}{\partial b} \left(\dot{b} - \boldsymbol{u} \cdot \boldsymbol{\nabla} b \right) + \frac{\partial \mathcal{F}}{\partial \phi} \left(\dot{\phi} - \boldsymbol{u} \cdot \boldsymbol{\nabla} \phi \right) \mathrm{d}V \\
&= \int_V \frac{\partial \mathcal{F}}{\partial b} \dot{b} + \frac{\partial \mathcal{F}}{\partial \phi} \dot{\phi} \, \mathrm{d}V - \int_V (\boldsymbol{u} \cdot \boldsymbol{\nabla} b) \frac{\partial \mathcal{F}}{\partial b} + (\boldsymbol{u} \cdot \boldsymbol{\nabla} \phi) \frac{\partial \mathcal{F}}{\partial \phi} \, \mathrm{d}V \\
&= \int_V \frac{\partial \mathcal{F}}{\partial b} \dot{b} + \frac{\partial \mathcal{F}}{\partial \phi} \dot{\phi} \, \mathrm{d}V - \int_V \boldsymbol{\nabla} \cdot (\boldsymbol{u} \mathcal{F}(b, \phi)) \, \mathrm{d}V,
\end{aligned} \tag{C5}
$$

since $\boldsymbol{\nabla} \cdot \boldsymbol{u} = 0$. By the divergence theorem we have

$$
\frac{\partial g_{\mathcal{F}}}{\partial t} = \int_V \frac{\partial \mathcal{F}}{\partial b} \dot{b} + \frac{\partial \mathcal{F}}{\partial \phi} \dot{\phi} \, \mathrm{d}V + \int_{\partial V} \boldsymbol{u} \cdot \boldsymbol{n} \, \mathcal{F}(b, \phi) \, \mathrm{d}S, \tag{C6}
$$

where ∂V is the boundary of V and $\boldsymbol{n}$ is the inward normal on ∂V. This forms an evolution equation for $g_{\mathcal{F}}$. Note that we choose an inward normal so that the final term is positive when fluid flows into V.

We now consider the specific choice $\mathcal{F}(b, \phi; B, \Phi) = I(b; B)I(\phi; \Phi)$ where, for a field $\psi(\boldsymbol{x}, t)$ defined in V, $I(\psi; \Psi)$ is the indicator function for the subset of V where $\psi(\boldsymbol{x}, t) > \Psi$, i.e.

$$
I(\psi; \Psi) = \begin{cases} 1 & \psi(\boldsymbol{x}, t) > \Psi \\ 0 & \psi(\boldsymbol{x}, t) \leqslant \Psi. \end{cases} \tag{C7}
$$

With this choice of $\mathcal{F}$, the function $g_{\mathcal{F}}$ is the volume of fluid in V with $b > B$ and $\phi > \Phi$. Furthermore $(\partial^2/\partial B \partial \Phi)g_{\mathcal{F}}$ is the 'volume density', i.e. $(\partial^2/\partial B \partial \Phi)g_{\mathcal{F}} \delta b \delta \phi$ is the volume of fluid in V with $B < b(\boldsymbol{x}, t) < B + \delta b$ and $\Phi < \phi(\boldsymbol{x}, t) < \Phi + \delta \phi$. This leads to the choice of name 'buoyancy–tracer volume distribution' for W.

We now simplify the right-hand side terms in (C6) for the choice $\mathcal{F}(b, \phi; B, \Phi) = I(b; B)I(\phi; \Phi)$. We have

$$
\begin{aligned}
\int_V \frac{\partial \mathcal{F}}{\partial b} \dot{b} \, \mathrm{d}V &= \int_V \dot{b} \, \delta(b(\boldsymbol{x}, t) - B) I(\phi; \Phi) \, \mathrm{d}V \\
&= \int_{S(B, \Phi)} \dot{b} \, \frac{\mathrm{d}S}{\partial b/\partial \boldsymbol{m}} \\
&= -\frac{\partial}{\partial B} \int_V \dot{b} \, I(b; B)I(\phi; \Phi) \, \mathrm{d}V,
\end{aligned} \tag{C8}
$$

where $S(B, \Phi)$ is the surface in V where $b(\boldsymbol{x}, t) = B$ and $\phi(\boldsymbol{x}, t) > \Phi$, and $\boldsymbol{m}$ is the normal to the surface $S(B, \Phi)$. Similarly,

$$
\int_V \frac{\partial \mathcal{F}}{\partial \phi} \dot{\phi} \, \mathrm{d}V = -\frac{\partial}{\partial \Phi} \int_V \dot{\phi} I(b; B)I(\phi; \Phi) \, \mathrm{d}V. \tag{C9}
$$

Then the evolution equation (C6) with the choice $\mathcal{F}(b, \phi; B, \Phi) = I(b; B)I(\phi; \Phi)$ gives the integral form (C10) of the evolution equation (C1), which governs the buoyancy–tracer

997 A48-35

cumulative volume distribution

$$\frac{\partial}{\partial t} \int_V I(b; B) I(\phi; \Phi) \, \mathrm{d}V = -\frac{\partial}{\partial B} \left[\int_V \dot{b} \, I(b; B) I(\phi; \Phi) \, \mathrm{d}V \right]$$

$$- \frac{\partial}{\partial \Phi} \left[\int_V \dot{\phi} \, I(b; B) I(\phi; \Phi) \, \mathrm{d}V \right]$$

$$+ \int_{\partial V} \boldsymbol{u} \cdot \boldsymbol{n} \, I(b; B) I(\phi; \Phi) \, \mathrm{d}S. \tag{C10}$$

The governing equation for the buoyancy-tracer volume distribution $W(B, \Phi; t)$ is obtained by taking $\partial^2 / \partial B \partial \Phi$ of (C10) to get

$$\frac{\partial}{\partial t} \int_V \delta(b(\boldsymbol{x}, t) - B) \delta(\phi(\boldsymbol{x}, t) - \Phi) \, \mathrm{d}V = -\frac{\partial}{\partial B} \left[\int_V \dot{b} \, \delta(b(\boldsymbol{x}, t) - B) \delta(\phi(\boldsymbol{x}, t) - \Phi) \, \mathrm{d}V \right]$$

$$- \frac{\partial}{\partial \Phi} \left[\int_V \dot{\phi} \, \delta(b(\boldsymbol{x}, t) - B) \delta(\phi(\boldsymbol{x}, t) - \Phi) \, \mathrm{d}V \right]$$

$$+ \int_{\partial V} \boldsymbol{u} \cdot \boldsymbol{n} \, \delta(b(\boldsymbol{x}, t) - B) \delta(\phi(\boldsymbol{x}, t) - \Phi) \, \mathrm{d}S. \tag{C11}$$

Since each integral is taken over the volume V, we are left with functions of B, Φ and t alone. With the definitions

$$W(B, \Phi; t) = \int_V \delta(b(\boldsymbol{x}, t) - B) \delta(\phi(\boldsymbol{x}, t) - \Phi) \, \mathrm{d}V, \tag{C12}$$

$$F_b(B, \Phi; t) = \int_V \dot{b} \, \delta(b(\boldsymbol{x}, t) - B) \delta(\phi(\boldsymbol{x}, t) - \Phi) \, \mathrm{d}V, \tag{C13}$$

$$F_\phi(B, \Phi; t) = \int_V \dot{\phi} \, \delta(b(\boldsymbol{x}, t) - B) \delta(\phi(\boldsymbol{x}, t) - \Phi) \, \mathrm{d}V, \tag{C14}$$

$$S(B, \Phi; t) = \int_{\partial V} \boldsymbol{u} \cdot \boldsymbol{n} \, \delta(b(\boldsymbol{x}, t) - B) \delta(\phi(\boldsymbol{x}, t) - \Phi) \, \mathrm{d}S, \tag{C15}$$

then (C11) can be written as

$$\frac{\partial W}{\partial t} = -\boldsymbol{\nabla}_{(B, \Phi)} \cdot \boldsymbol{F} + S, \tag{C16}$$

where $\boldsymbol{F} = (F_b, F_\phi)$, which completes the derivation.

Appendix D. Numerical method for identifying the accumulation region of (b, ϕ)-space

In § 4.6 we introduce a partitioning of buoyancy-tracer space into three regions. Undiluted plume fluid corresponds with regions of buoyancy-tracer space where $M(b, \phi; t) < 0$ in QSS (see § 4.5). Mixed fluid in the stratified layer is identified by regions of (b, ϕ)-space with $M(b, \phi; t) > 0$. Mixed fluid is further partitioned by a threshold value $m^*(t)$ such that $0 < M \leqslant m^*$ identifies newly generated mixed fluid, where plume fluid is actively mixing with the environment in the plume cap; and $M > m^*$ identifies plume fluid which has mixed with the environment and is accumulating in the radially spreading intrusion.

The threshold $m^*(t)$ is chosen to minimise the total mixing flux convergence $f(m; t)$ of the transport region $\mathcal{T} = \{0 < M \leqslant m^*\}$, i.e. $m^*(t)$ is the value m that minimises $|f(m; t)|$ where

$$f(m; t) = \int_{\{0 < M \leqslant m\}} \frac{\partial W}{\partial t} - S \, \mathrm{d}b \, \mathrm{d}\phi = - \int_{\{0 < M \leqslant m\}} \boldsymbol{\nabla}_{(b,\phi)} \cdot \boldsymbol{F} \, \mathrm{d}b \, \mathrm{d}\phi, \qquad \text{(D1)}$$

so that the volume that enters the region $\mathcal{T}$ is approximately equal to the volume leaving $\mathcal{T}$. The region $\mathcal{A}$ which represents the remainder of the mixed fluid must then capture the accumulation of mixed fluid.

The numerical implementation of this method involves, at each time step k, the following steps:

(i) identify the current maximum value of M throughout buoyancy-tracer space, denoted $\mathcal{M} = \max_{i,j} M_{ij}(t_k)$;
(ii) for each of N_M test values of M, $m = 0, \ldots, \mathcal{M}$, calculate

$$f(m; t_k) \approx \sum_{i,j \mid 0 < M_{ij} \leqslant m} \left[\frac{W_{ij}(t_{k+1}) - W_{ij}(t_k)}{\Delta t} - S_{ij}(t_k) \right]; \qquad \text{(D2)}$$

(iii) identify the test value $\tilde{m}(t_k)$ which minimises $f(m; t_k)$.

Then, once a threshold $\tilde{m}(t_k)$ has been chosen for each timestep t_k, the final threshold $m^*(t)$ is chosen by applying a rolling average with an appropriate number of timesteps. We choose $N_M = 200$ and a rolling average width of 10 timesteps. The motivation for applying a rolling average is to smooth the threshold $m^*(t)$ so that the regions $\mathcal{T}$ and $\mathcal{A}$ do not grow and shrink dramatically in response to short-term changes in the flux divergence.

Figure 19(*a*) shows the total flux convergence $f(m; t)$ for all times post-penetration and figure 19(*b*) shows the corresponding preliminary thresholds $\tilde{m}(t)$ and the final thresholds $m^*(t)$. The total mixing flux convergence of class T for the preliminary and final thresholds over time is shown in figure 19(*c*), indicating the (generally small) error introduced by smoothing the thresholds.

Appendix E. Potential energy budget

In §5.1 we introduce the perturbation PE $E_p = \frac{1}{2}\langle b'^2 \rangle$ where b' is the departure from the initial linear stratification, i.e. $b(\boldsymbol{x}, t) = b'(\boldsymbol{x}, t) + z$. This form of the PE may be derived from (2.15) of Holliday & McIntyre (1981) under the assumption of a constant buoyancy gradient in the initial stratified environment. The perturbation PE may be treated as a proxy for APE. To examine the mixing processes in the plume we wish to identify the primary sink of E_p in order to calculate the mixing efficiency. We must therefore form a budget equation for the perturbation PE E_p.

We start with the governing equations (2.1)–(2.3) including the SGS terms and drop the hat notation. Substituting the buoyancy decomposition defined above, $b = z + b'$, the buoyancy evolution equation becomes

$$\frac{\partial b'}{\partial t} + w + \boldsymbol{u} \cdot \boldsymbol{\nabla} b' = \frac{1}{RePr} \nabla^2 b' + \boldsymbol{\nabla} \cdot \left(\kappa_{SGS}^{(b)} \boldsymbol{\nabla} b' \right) + \frac{\partial}{\partial z} \kappa_{SGS}^{(b)} + f_b. \qquad \text{(E1)}$$

Now, multiplying by the buoyancy departure from the initial stratification b' and volume averaging over a fixed volume V gives

$$\frac{\mathrm{d}E_p}{\mathrm{d}t} = \int_{\partial V} \left[\frac{1}{RePr} + \kappa_{SGS}^{(b)} \right] b' \boldsymbol{\nabla} b' \cdot \mathrm{d}S - \bar{\chi} - \overline{J_b} - \left\langle b' \frac{\partial \kappa_{SGS}^{(b)}}{\partial z} \right\rangle, \qquad \text{(E2)}$$
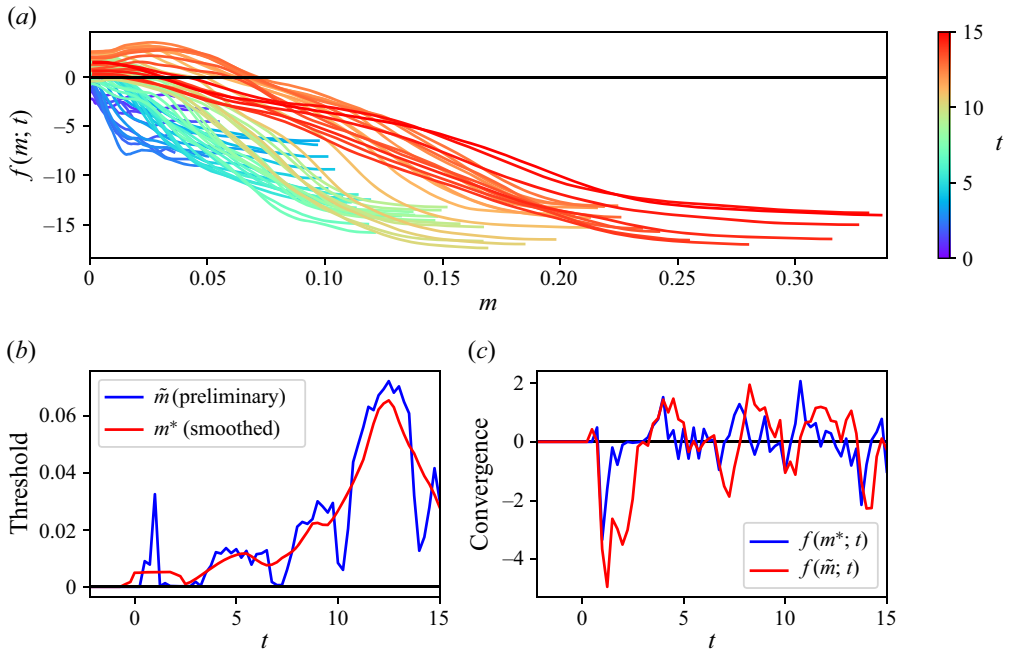
(*a*)

Figure 19. (*a*) Total flux divergence $f(m;t)$ defined in (D1) and the resulting preliminary and smoothed threshold choice in (*b*). Error in f from smoothing process shown in (*c*).

where $\langle \cdot \rangle$ denotes a volume average over V. Note that the term involving f_b has been neglected since the buoyancy forcing vanishes above the forcing region and we will apply this perturbation PE budget in the stratified layer. The first term on the left-hand side represents the diffusive buoyancy flux across the boundary ∂V, which is non-zero only where the plume penetrates the stratified layer. The second term is the volume-averaged buoyancy variance dissipation rate

$$\bar{\chi} = \left\langle \left(\frac{1}{RePr} + \kappa_{SGS}^{(b)} \right) |\nabla b'|^2 \right\rangle, \qquad (E3)$$

which represents the primary sink of perturbation PE. The third term is the volume averaged buoyancy flux

$$\overline{J_b} = \langle b'w \rangle \qquad (E4)$$

which represents an exchange between kinetic and PE. The last term captures the effect of the spatially varying SGS diffusivity acting on the background stratification.

REFERENCES

ALFONSI, G. 2011 On direct numerical simulation of turbulent flows. *Appl. Mech. Rev.* **64** (2), 020802.
ANSONG, J.K., KYBA, P.J. & SUTHERLAND, B.R. 2008 Fountains impinging on a density interface. *J. Fluid Mech.* **595**, 115–139.
ANSONG, J.K. & SUTHERLAND, B.R. 2010 Internal gravity waves generated by convective plumes. *J. Fluid Mech.* **648**, 405–434.
BRIGGS, G.A. 1965 A plume rise model compared with observations. *J. Air Pollut. Control Assoc.* **15** (9), 433–438.

CARAZZO, G., KAMINSKI, E. & TAIT, S. 2008 On the rise of turbulent plumes: quantitative effects of variable entrainment for submarine hydrothermal vents, terrestrial and extra terrestrial explosive volcanism. *J. Geophys. Res.* **113** (B9), 2007JB005458.

CHEMEL, C. & STAQUET, C. 2007 A formulation of convective entrainment in terms of mixing efficiency. *J. Fluid Mech.* **580**, 169–178.

CHEN, C.H. & BHAGANAGAR, K. 2023 Energetics of buoyancy-generated turbulent flows with active scalar: pure buoyant plume. *J. Fluid Mech.* **954**, A23.

DAUHUT, T., CHABOUREAU, J.-P., ESCOBAR, J. & MASCART, P. 2015 Large-eddy simulations of hector the convector making the stratosphere wetter. *Atmos. Sci. Lett.* **16** (2), 135–140.

DAUHUT, T., CHABOUREAU, J.-P., HAYNES, P.H. & LANE, T.P. 2018 The mechanisms leading to a stratospheric hydration by overshooting convection. *J. Atmos. Sci.* **75** (12), 4383–4398.

DAVIES WYKES, M.S. & DALZIEL, S.B. 2014 Efficient mixing in stratified flows: experimental study of a Rayleigh–Taylor unstable interface within an otherwise stable stratification. *J. Fluid Mech.* **756**, 1027–1057.

DAVIES WYKES, M.S., HUGHES, G.O. & DALZIEL, S.B. 2015 On the meaning of mixing efficiency for buoyancy-driven mixing in stratified turbulent flows. *J. Fluid Mech.* **781**, 261–275.

DEBONIS, J.R. 2019 WRLES: wave resolving large-eddy simulation code, theory and usage. *NASA/TM* 2019-220192.

DEVENISH, B.J., ROONEY, G.G. & THOMSON, D.J. 2010 Large-eddy simulation of a buoyant plume in uniform and stably stratified environments. *J. Fluid Mech.* **652**, 75–103.

DODA, T., ULLOA, H.N., RAMÓN, C.L., WÜEST, A. & BOUFFARD, D. 2023 Penetrative convection modifies the dynamics of downslope gravity currents. *Geophys. Res. Lett.* **50** (2), e2022GL100633.

GARCÍA-VILLALBA, M. & DEL ÁLAMO, J.C. 2011 Turbulence modification by stable stratification in channel flow. *Phys. Fluids* **23** (4), 045104.

GREGG, M.C., D'ASARO, E.A., RILEY, J.J. & KUNZE, E. 2018 Mixing efficiency in the ocean. *Annu. Rev. Mar. Sci.* **10**, 443–473.

HERRMANN, M., SOMOT, S., SEVAULT, F., ESTOURNEL, C. & DÉQUÉ, M. 2008 Modeling the deep convection in the northwestern Mediterranean Sea using an eddy-permitting and an eddy-resolving model: case study of winter 1986–1987. *J. Geophys. Res.* **113** (C4), C04011.

HOLLIDAY, D. & MCINTYRE, M.E. 1981 On potential energy density in an incompressible, stratified fluid. *J. Fluid Mech.* **107**, 221–225.

HOWLAND, C.J., TAYLOR, J.R. & CAULFIELD, C.P. 2020 Mixing in forced stratified turbulence and its dependence on large-scale forcing. *J. Fluid Mech.* **898**, A7.

HUNT, G.R. & BURRIDGE, H.C. 2015 Fountains in industry and nature. *Annu. Rev. Fluid Mech.* **47** (1), 195–220.

HUNT, G.R. & KAYE, N.B. 2005 Lazy plumes. *J. Fluid Mech.* **533**, 329–338.

IVEY, G.N., WINTERS, K.B. & KOSEFF, J.R. 2008 Density stratification, turbulence, but how much mixing? *Annu. Rev. Fluid Mech.* **40** (1), 169–184.

JENSEN, E.J., ACKERMAN, A.S. & SMITH, J.A. 2007 Can overshooting convection dehydrate the tropical tropopause layer? *J. Geophys. Res.: Atmos.* **112**, D11209.

KURBATSKII, A.F. 2001 Computational modeling of the turbulent penetrative convection above the Urban Heat Island in a stably stratified environment. *J. Appl. Meteorol.* **40** (10), 1748–1761.

LIST, E.J. 1982 Turbulent jets and plumes. *Annu. Rev. Fluid Mech.* **14** (1), 189–212.

LORENZ, E.N. 1955 Available potential energy and the maintenance of the general circulation. *Tellus* **7** (2), 157–167.

LUMLEY, J.L. & NEWMAN, G.R. 1977 The return to isotropy of homogeneous turbulence. *J. Fluid Mech.* **82** (1), 161–178.

MARSHALL, J. & SCHOTT, F. 1999 Open-ocean convection: observations, theory, and models. *Rev. Geophys.* **37** (1), 1–64.

MASADA, Y., YAMADA, K. & KAGEYAMA, A. 2013 Effects of penetrative convection on solar dynamo. *Astrophys. J.* **778** (1), 11.

MORTON, B.R. 1959 Forced plumes. *J. Fluid Mech.* **5** (1), 151–163.

MORTON, B.R., TAYLOR, G.I. & TURNER, J.S. 1956 Turbulent gravitational convection from maintained and instantaneous sources. *Proc. R. Soc. Lond.* A **234** (1196), 1–23.

PAPANICOLAOU, P.N. & LIST, E.J. 1988 Investigations of round vertical turbulent buoyant jets. *J. Fluid Mech.* **195**, 341–391.

PELTIER, W.R. & CAULFIELD, C.P. 2003 Mixing efficiency in stratified shear flows. *Annu. Rev. Fluid Mech.* **35** (1), 135–167.

PENNEY, J., MOREL, Y., HAYNES, P.H., AUCLAIR, F. & NGUYEN, C. 2020 Diapycnal mixing of passive tracers by Kelvin–Helmholtz instabilities. *J. Fluid Mech.* **900**, A26.

PHAM, M.V., PLOURDE, F. & DOAN, K.S. 2007 Direct and large-eddy simulations of a pure thermal plume. *Phys. Fluids* **19** (12), 125103.

PLUMB, R.A. 2007 Tracer interrelationships in the stratosphere. *Rev. Geophys.* **45**, RG4005.

RANDEL, W.J. & JENSEN, E.J. 2013 Physical processes in the tropical tropopause layer and their roles in a changing climate. *Nat. Geosci.* **6** (3), 169–176.

VAN REEUWIJK, M., SALIZZONI, P., HUNT, G.R. & CRASKE, J. 2016 Turbulent transport and entrainment in jets and plumes: a DNS study. *Phys. Rev. Fluids* **1**, 074301.

DE ROOY, W.C., BECHTOLD, P., FRÖHLICH, K., HOHENEGGER, C., JONKER, H., MIRONOV, D., PIER SIEBESMA, A., TEIXEIRA, J. & YANO, J.-I. 2013 Entrainment and detrainment in cumulus convection: an overview. *Q. J. R. Meteorol. Soc.* **139** (670), 1–19.

SHABBIR, A. & GEORGE, W.K. 1994 Experiments on a round turbulent buoyant plume. *J. Fluid Mech.* **275**, 1–32.

SINGH, H.P., ROXBURGH, I.W. & CHAN, K.L. 1994 Three-dimensional simulation of penetrative convection-penetration above a convection zone. *Astron. Astrophys.* **281** (2), L73–L76.

TAYLOR, J.R. 2008 Numerical simulations of the stratified oceanic bottom layer. PhD thesis, University of California, San Diego.

TEXTOR, C., GRAF, H.-F., HERZOG, M. & OBERHUBER, J.M. 2003 Injection of gases into the stratosphere by explosive volcanic eruptions. *J. Geophys. Res.* **108** (D19), 4606.

TURNER, J.S. 1966 Jets and plumes with negative or reversing buoyancy. *J. Fluid Mech.* **26** (4), 779–792.

ULSES, C., ESTOURNEL, C., FOURRIER, M., COPPOLA, L., KESSOURI, F., LEFÈVRE, D. & MARSALEIX, P. 2021 Oxygen budget of the north-western Mediterranean deep- convection region. *Biogeosciences* **18** (3), 937–960.

VREUGDENHIL, C.A. & TAYLOR, J.R. 2018 Large-eddy simulations of stratified plane couette flow using the anistropic minimum-dissipation model. *Phys. Fluids* **30** (8), 085104.